SHELL STRUCTURE AND ORBIT BIFURCATIONS IN FINITE FERMION SYSTEMS

A. G. Magner[1], I. S. Yatsyshyn[1], K. Arita[2], M. Brack[3]

[1] *Institute for Nuclear Research, 03680, Kyiv, Ukraine*

[2] *Physic Department, Nagoya Institute of Technology, 466-8555, Nagoya, Japan*

[3] *Institute for Theoretical Physics, University of Regensburg, D-93040, Regensburg, Germany*

arXiv:1012.0832v3 [nucl-th] 7 Dec 2010

Abstract

We first give an overview of the shell-correction method which was developed by V. M. Strutinsky as a practicable and efficient approximation to the general selfconsistent theory of finite fermion systems suggested by A. B. Migdal and collaborators. Then we present in more detail a semiclassical theory of shell effects, also developed by Strutinsky following original ideas of M. Gutzwiller. We emphasize, in particular, the influence of orbit bifurcations on shell structure. We first give a short overview of semiclassical trace formulae, which connect the shell oscillations of a quantum system with a sum over periodic orbits of the corresponding classical system, in what is usually called the "periodic orbit theory". We then present a case study in which the gross features of a typical double-humped nuclear fission barrier, including the effects of mass asymmetry, can be obtained in terms of the shortest periodic orbits of a cavity model with realistic deformations relevant for nuclear fission. Next we investigate shell structures in a spheroidal cavity model which is integrable and allows for far-going analytical computation. We show, in particular, how period-doubling bifurcations are closely connected to the existence of the so-called "superdeformed" energy minimum which corresponds to the fission isomer of actinide nuclei. Finally, we present a general class of radial power-law potentials which approximate well the shape of a Woods-Saxon potential in the bound region, give analytical trace formulae for it and discuss various limits (including the harmonic oscillator and the spherical box potentials).

PACS: 21.60. Ev, 21.60. Cs, 24.10 Pa, 24.75. +i

February 16, 2022

1 INTRODUCTION

This paper is devoted to the memory of A. B. Migdal. Our first aim here is to review the shell-correction method (SCM) which was first introduced by Strutinsky on a phenomenological basis [1] and then microscopically founded [2] on Migdal's theory for strongly interacting finite fermion systems [3]. Our second aim is the discussion of a semiclassical theory of shell effects, using the so-called periodic orbit theory (POT) (see [4] for an introductory text book). It provides us with a nice tool for answering, sometimes even analytically, some fundamental questions asked [5, 6, 7] by Strutinsky: Why are nuclei deformed? What are the physical origins of the double-humped fission barrier and, in particular, of the existence of the isomer minimum? His idea was to use the POT for a deeper understanding, based on classical pictures, of the origin of nuclear shell structure and its relation to a possible chaotic nature of the nucleons' dynamics. We shall present some applications of the POT to nuclear deformation energies and discuss in more detail the relation of bifurcations of periodic orbits with pronounced shell effects.

According to the SCM, the oscillating part of the total energy of a finite fermion system, the so-called shell-correction energy δE, is associated with an inhomogeneity of the single-particle (s.p.) energy levels near the Fermi surface. Its existence in dense fermion systems is a basic point of Landau's quasi-particle theory of infinite Fermi liquids [8, 9], as extended to self-consistent finite fermion systems by Migdal and collaborators [3, 10]. This is schematically illustrated in Fig. 1, where the s.p. level spectrum of a bound nucleus is shown in two extremal situations. Depending on the level density at the Fermi energy – and with it the shell-correction energy δE – being a maximum or a minimum, the nucleus is particularly unstable or stable, respectively. This situation varies with particle numbers and deformations of the nucleus. In consequence, the shapes of stable nuclei depend strongly on particle numbers and deformations. This is illustrated in Fig. 2. Here the shell correction δE of the neutrons is shown as function of the neutron number N and the deformation parameter η of a Woods-Saxon potential [11] with spheroidal shape, η being the ratio of the semi-axes. If we fix the neutron number N, e.g. $N = 150$, and increase the deformation η, we meet the first minimum (ground state) at about $\eta \sim 1.25$ and the next one (isomeric state) at much larger deformations $\eta \sim 1.9 - 2.1$. The experimental data corresponding to these deformations are shown in Fig. 2 by the heavy dots.

The SCM was successfully used to describe nuclear masses and deformation energies and, in particular, fission barriers of heavy nuclei. For an early review by Strutinsky's group, in which also the miscroscopic foundations of the SCM are discussed, see Ref. [12]. (We refer to Sect. 3.2 for a further discussion of fission barriers.)

In Sect. 2, we will give a short review of the SCM and its foundation on the basis of a selfconsistent theory of finite interacting fermion systems.

Sect. 3 is devoted to the semiclassical theory of shell effects. The POT is based on Gutzwiller's semiclassical trace formula for the level density for a Hamiltonian system with isolated orbits [13] and its extensions to systems with continuous symmetries [4, 5, 14, 15, 16, 17]. It allows one to relate both the oscillating part of the level density and the shell-correction energy of a quantum system to the shortest periodic orbits (POs) of the corresponding classical Hamiltonian system. Thus, one can often explain pronounced shell effects by the role of particular short POs. As an early example, taken from Ref. [5], the heavy bars in Fig. 2 are the predictions of the POT for the loci of the ground-state minima, using the shortest POs in a spheroidal cavity. Bifurcations of POs under the variation of a deformation parameter or the (Fermi) energy can have noticeable effects for the shell structure [5, 6, 7, 18, 19, 20, 21].

In Sect. 3.1, we will present the structure of semiclassical trace formula and discuss a general method of treating bifurcations in the POT, using the catastrophe theory of Fedoryuk and Maslov for caustic and turning-point problems [22, 23, 24, 25].

In Sect. 3.2, we review the semiclassical description [26] of a typical nuclear fission barrier in terms of the shortest periodic orbits, employing a cavity model with the realistic shape parameterization developed in [12]. In particular, the effect of left-right asymmetric deformations on the height of the outer fission barrier will be discussed. Isochronous bifurcations of the shortest orbits are treated here in a uniform approximation employing a suitable normal form for the action function.

In Sect. 3.3, we use the spheroidal cavity [5, 19, 20, 27] as a simple integrable model that allows to study semiclassically the shell structure related to the 'super-deformed' energy minimum which in realistic actinide nuclei corresponds to the fission isomers. Strutinsky's prediction concerning the importance of the enhancement of the shell structure owing to period-doubling bifurcations of three-dimensional POs from simple equatorial (EQ) orbits in the spheroidal cavity model [5] will be discussed.

In Sect. 3.4, we shall study a radial power-law potential [28], which is a good approximation to the familiar Woods-Saxon potential for nuclei in the spatial domain where the particles are bound. We shall establish generalised trace formulae for this potential and discuss various limits to other known potentials.

The paper is summarized in Sect. 4, where we also present some conclusions and plans for future research. Some technical details of our POT calculations are given in the Appendix.

2 THE SHELL-CORRECTION METHOD

In 1966, Strutinsky achieved a far-reaching break-through [29], following basically Migdal's theory of finite fermion systems[2, 3]. Until then, many attempts had been made to incorporate quantum shell effects in the calculation of nuclear deformation energies. But they all failed in reproducing the fission barriers of actinide nuclei and details such as, e.g., the left-right asymmetry of the nascent fission fragments [30]. Summing the s.p. energies of a deformed shell model (like the Nilsson model [31]) up to the Fermi energy failed at larger deformations. There was a need to renormalize the wrong average part of the s.p. energy sum. Knowing that the smooth part of the nuclear binding energy could be well described by the phenomenological LDM [32, 33, 34] (or droplet model [35]), Strutinsky wrote the total nuclear energy as [1, 12]

$$E_{tot} = E_{LDM} + \delta E\,, \tag{1}$$

where E_{LDM} is the LDM energy and δE the so-called *"shell-correction energy"* which contains the fluctuating part of the s.p. energy sums for the neutrons:

$$\delta E = \sum_{n=1}^{N/2} E_n - \langle \sum_{n=1}^{N/2} E_n \rangle\,, \tag{2}$$

and similarly for the protons. Both parts of the total energy (1) depend on the neutron and proton numbers N and Z, as well as on the nuclear deformation which has to be suitably parameterized both in the LDM and the shell model. While it had been a wide-spread belief that the shell-correction δE was important only for spherical nuclei and would vanish at larger deformations, Strutinsky was convinced that shell effects play an important role also at larger deformations and lead, in fact, to new magic numbers corresponding to deformed systems with increased local stability [1].

For the determination of the smooth parts $\langle \sum_{n=1}^{N/2} E_n \rangle$ in (2), Strutinsky designed a very ingenious averaging method [1, 29] which has been termed the *"Strutinsky averaging* (or *smoothing*) *method"*. It consists of a Gaussian convolution of the s.p. energy spectrum, modified by the so-called *"curvature corrections"* in such a way that the result does not depend on the energy averaging width γ (at least within a finite interval of γ of the order of the main shell spacing) and at the same time reproduces the true average level density which is found, e.g., from the extended Thomas-Fermi (ETF) model, or from the Weyl expansion in the case of billiard or cavity models (see, e.g., [4], Chap. 4, for details).

Strutinsky applied the SCM to the calculation of fission barriers[1, 29], employing the Nilsson model. For a typical actinide nucleus he obtained a second minimum in the deformation energy, lying above the ground state by about 3 MeV, at a deformation much larger than that of the

ground state. This was, in fact, the physical explanation of the *fission isomer* which had been known experimentally [36] since 1962, but not understood theoretically. Strutinsky presented this result at the Symposium *"Nuclides far off the stability line"* in Lysekil (Sweden) [37] in 1966 and, being a member of Migdal's theory group, he immediately became famous. He was then invited to the NBI in Copenhagen, in order to extend his calculations of fission barriers on a larger scale, employing more realistic shell-model potentials, which led to the team work published in Ref. [12].

The SCM was soon taken up by many groups of the international scientific community and often also called the *"microscopic-macroscopic"* method [35, 38]. Various combinations of nuclear shell models and liquid drop(let) models were used. Still today, the shell-correction method is being used world wide for calculations of nuclear masses and deformation energies, and it persists to yield the most accurate nuclear mass tables, ground-state and isomeric deformations and, in particular, fission barriers.

The Strutinsky averaging used for the second term in (2) is done in energy space and leads, within a sufficient numerical accuracy, to the same results as the ETF model ([39], see also [4], Ch. 4.7). However, it is formally not completely consistent with the particle-number averaging that is implicitly done in the standard least-square fits to the LDM which defines the smooth part of the total nuclear energy (1). Already early, alternative particle-number averagings were investigated in [40]. Using semiclassical POT arguments, the difference between energy and particle-number averaging was understood [41, 42] as a symmetry correction which becomes especially significant for spherical nuclear shapes (particularly in the harmonic oscillator model). Smaller discrepancies for the deformed Fermi systems in the resulting shell-correction energies persist, however, as discussed in [41, 42, 43]. This point is thus still an object of current debate.

The decomposition of the total nuclear energy into a smooth and an oscillating part in (1) may at first glance look like a rather phenomenological ansatz. In particular, since the oscillating part is taken from the sum of occupied s.p. energies of the nucleons, one may argue that it cannot be correct, since this sum is well known not to represent the total energy in a self-consistent microscopic theory (where it double-counts the potential energy if the interaction does not depend on the density). However, it was soon realized that (1) is nevertheless correct even within a self-consistent microscopic theory. This was pointed out, amongst others, by Bethe [44] who therefore termed (1) the *"Strutinsky energy theorem"*. It can be rigorously proved that the oscillating part of the correct total energy is, indeed, contained in the s.p. sums; the proof is simply based on the variational principle that governs the self-consistent mean-field theories (see, e.g., [4], App. A.3), and it applies also to density-dependent nuclear interactions [44]. This was soon demonstrated by

the Strutinsky group [2] to hold also within the Migdal theory [3]. At this point it may be worth mentioning that the Migdal theory has been used explicitly to calculate energy shell corrections for doubly magic nuclei, investigating the so-called "lead anomaly" (i.e., in particular for nuclei around ^{208}Pb) [45].

The Strutinsky energy theorem (1) was later tested numerically using the Hartree-Fock (HF) approach with effective Skyrme interactions. By extracting a self-consistently Strutinsky-averaged part of the total HF energy (which is ideally represented by the LDM energy E_{LDM}), the first-order oscillating term was, indeed, found to be correctly represented by the shell-correction energy (2) evaluated in terms of the energy spectrum of the *averaged* self-consistent HF potentials (which are ideally represented by the shell-model potentials). The remaining higher-order terms were found to be relatively small, less than ~ 1 MeV in all (not too small) nuclei [46].

The shell-correction method is thus a well-established practical approximation to a self-consistent microscopic theory and applicable to any bound many-fermion system. It has, e.g., been applied to metal clusters by many groups (see [47, 48, 49, 50] for a few representative references). For semiconductor quantum dots, the Strutinsky energy theorem and shell-corrections to the Coulomb interaction energy were discussed in [51].

3 SEMICLASSICAL THEORY OF SHELL STRUCTURE

3.1 SEMICLASSICAL TRACE FORMULAE

In the semiclassical trace formula of Gutzwiller [13] that connects the quantum-mechanical density of states with a sum over POs of the classical system, divergences arise at critical deformations where bifurcations of POs occur or where symmetry breaking (or restoring) transitions take place. At these points the standard stationary-phase method (standard SPM or SSPM), used in the semiclassical (asymptotical) evaluation of the trace integrals, breaks down. Various ways of avoiding these divergences have been suggested using uniform approximations (see [4], Sec. 6). Presently, we shall discuss the evaluation of trace integrals in the phase-space representation, following mainly the presentations in [18, 19, 20, 21].

The essence of a semiclassical trace formula is to relate the oscillating part of the level density of a quantum Hamiltonian system to the periodic orbits of the corresponding classical system. The level density $g(E)$ can be obtained from the semiclassical Green's function by taking the imaginary

part of its trace in phase space variables, see [21], also the references therein,

$$\begin{aligned} g(E) &= \sum_n \delta\left(E - E_n\right) \simeq \mathrm{Re} \sum_{CT} \int \frac{\mathrm{d}\mathbf{r}'\mathrm{d}\mathbf{p}''}{(2\pi\hbar)^3}\, \delta\left[E - H(\mathbf{r}'', \mathbf{p}'')\right] \\ &\times \left|\mathcal{J}_{CT}\right|^{1/2} \exp\left[\frac{i}{\hbar}\,\Phi_{CT} - i\frac{\pi}{2}\mu_{CT}\right], \end{aligned} \tag{3}$$

where the delta function imposes the energy conservation of the particle motion along the classical trajectory (CT) in the potential well of the Hamiltonian $H(\mathbf{r}, \mathbf{p})$. Φ_{CT} is the action phase,

$$\Phi_{CT} = S_{CT}(\mathbf{r}', \mathbf{r}'', E) - \mathbf{p}'' \cdot (\mathbf{r}'' - \mathbf{r}')\,; \qquad S_{CT}(\mathbf{r}', \mathbf{r}'', E) = \int_{\mathbf{r}'}^{\mathbf{r}''} \mathrm{d}\mathbf{r} \cdot \mathbf{p}(\mathbf{r})\,. \tag{4}$$

The second equation yields the action along the CT. The Maslov phase μ_{CT} is determined by the number of caustic and turning points within the catastrophe theory by Fedoryuk and Maslov [21, 22, 23, 24]. In (3), $\mathcal{J}_{CT}(\mathbf{p}'_\perp, \mathbf{p}''_\perp)$ is the Jacobian of the transformation from the momentum perpendicular to the CT $\mathbf{p}'_\perp$ at the initial point $\mathbf{r}'$ to the perpendicular momentum $\mathbf{p}''_\perp$ at the final point $\mathbf{r}''$ of the CT. One may divide the level density into a smooth and an oscillating part:

$$g(E) = \widetilde{g}\,(E) + \delta g(E)\,. \tag{5}$$

The smooth part $\widetilde{g}\,(E)$ is, to leading order in $1/\hbar$, given [52] by the direct (zero-time or zero-length) trajectories which yield the Thomas-Fermi (TF) results. Except for one-dimensional systems, higher $\hbar$ corrections contribute to it which may be calculated within the ETF model (or the Weyl expansion for billiards) [4], so that we can make the identification

$$\widetilde{g}\,(E) = g_{ETF}(E)\,. \tag{6}$$

For the calculation of the oscillating component $\delta g(E)$, we apply the stationary phase method to the integration over the phase space variables. The stationary phase condition reads:

$$\left(\frac{\partial \Phi_{CT}}{\partial \mathbf{p}''}\right)^* \equiv (\mathbf{r}' - \mathbf{r}'')^* = 0, \qquad \left(\frac{\partial \Phi_{CT}}{\partial \mathbf{r}'}\right)^* \equiv -\left(\mathbf{p}' - \mathbf{p}''\right)^* = 0\,, \tag{7}$$

and is nothing but a condition for CT to be periodic. In the presence of continuous symmetries, the stationary points form a family of periodic orbits (POs) which cover a ($\mathcal{K}$+1)-dimensional submanifold Υ_{po} of phase space (denoted Γ_{po} in Ref. [4] and further references cited therein), whereby $\mathcal{K}$ is the degeneracy of the PO family. The integration over Υ_{po} must be performed exactly. In integrable systems, it is advantageous to transform phase space variables from Cartesian to action-angle variables (see, e.g., [16, 17]). Then the action Φ is a function only of the action variables, and the integrations over the cyclic angle variables are exactly carried out. Integrating over the remaining action variables using the standard SPM (under the existence of additional symmetries

like SU(3) or O(4), one of which can also be performed exactly), one obtains the so called Berry-Tabor trace formula [16].

For solving bifurcation problems in integrable and non-integrable systems, more exact integrations are required. In the SPM, after performing the exact integrations over Υ_{po}, one uses an expansion of the action phase $\Phi_{\rm CT}$ in phase space variables $\xi = \{\mathbf{r}', \mathbf{p}''\}_\perp$ perpendicular to Υ_{po} in the integrand of (3) over ξ near the stationary point ξ^*,

$$\Phi_{\rm CT}(\xi) = \Phi_{po} + \frac{1}{2}\Phi''_{\rm po}(\xi^*)(\xi - \xi^*)^2 + \frac{1}{6}\Phi'''_{po}(\xi^*)(\xi - \xi^*)^3 + \ldots, \quad \Phi_{po} = \Phi^*_{\rm CT} = \Phi_{\rm CT}(\xi^*)\,. \tag{8}$$

To demonstrate the key point of our derivations of the trace formula, we consider here only one (one-dimensional) variable, called ξ again, from the phase space integration variables in (3), on which we meet a bifurcation (catastrophe) point in applying the SPM. (We shall give comments if this might lead to a misunderstanding.) In the standard SPM, the above expansion is truncated at the 2nd order term and the integration over the variable ξ is extended to $\pm\infty$. The integration can be performed analytically and yields a Fresnel integral, see e.g. [4], Sect. 2.7, Eq. (2.169).

However, one meets singularities using the standard SPM which are related to zeros or infinities of $\Phi''_{po}(\xi^*)$ (or of eigenvalues of the corresponding matrix in the case of several integration variables ξ) while $\Phi'''_{po}(\xi^*)$ remains finite in the simplest case. These singularities occur when a PO (isolated or family) undergoes a bifurcation at the stationary point ξ^* under the variation of some parameter (e.g., energy or deformation). The Fresnel integrals of the standard SPM sketched above will then diverge. In order to avoid such singularities, we observe that the bifurcation problem is similar to the caustic singularity considered by Fedoryuk within the catastrophe theory [22, 24], adopted to its specific position at the edge of the phase-space volume accessible for the classical motion (see also Appendix A in [21]). Therefore, we employ what we call the "improved SPM", in short: ISPM [18, 19, 20, 21]. Hereby the integration over ξ in (3) is restricted to the *finite limits* defined by the classically allowed phase space region through the energy-conserving delta function in the integrand of (3). The expansion (8) of the action phases and similarly of the amplitudes in (3) is generally used up to the second- and zero-order terms, respectively, and if necessary, to higher order terms in $\xi - \xi^*$.

In the simplest version of ISPM, the expansion of the phase is truncated at 2nd order, keeping the finite integration limits ξ_- and ξ_+ given by the accessible region of the classical motion in (3). It will lead to a factor like

$$e^{i\Phi_{\rm po}/\hbar}\int_{\xi_-}^{\xi_+} \exp\left[\frac{i}{2\hbar}\Phi''_{po}\,(\xi - \xi^*)^2\right] {\rm d}\xi \propto \frac{1}{\sqrt{\Phi''_{po}}}\; e^{i\Phi_{po}/\hbar}\; {\rm erf}\left[\mathcal{Z}_-, \mathcal{Z}_+\right], \tag{9}$$

where $\mathrm{erf}(z_1, z_2)$ is the generalized error function with complex arguments

$$\mathrm{erf}(z_1, z_2) = \frac{2}{\sqrt{\pi}} \int_{z_1}^{z_2} e^{-z^2} \mathrm{d}z, \quad \mathcal{Z}_\pm = (\xi_\pm - \xi^*) \sqrt{-\frac{i}{2\hbar} \Phi''_{po}} \,. \tag{10}$$

Note that the above expression (9) has no divergence at the bifurcation point where $\Phi''_{po}(\xi^*) = 0$, since the error function (10) also goes to zero linearly in $\sqrt{\Phi''_{po}}$ [cf. the second equation in (10)], which keeps the result finite. [For the case of several variables ξ for which we find zeros or infinities of eigenvalues of the matrix $\Phi''_{po}(\xi^*)$, we diagonalize this matrix and reduce the Fresnel-like integrals to products of error functions similar to (9).]

This procedure is proved to be valid in the semiclassical limit by the Maslov-Fedoryuk theorem [22, 23, 24]. In this way, we can derive contributions from each periodic orbit free of divergences at any bifurcation point, and the oscillating part of the level density can be approximated by the following *semiclassical trace formula*:

$$\begin{aligned} \delta g(E) &\simeq \delta g_{scl}(E) = \sum_{po} \delta g^{\mathrm{scl}}_{po}(E) \,, \qquad \text{with} \\ \delta g^{\mathrm{scl}}_{po}(E) &= \mathrm{Re} \left\{ \mathcal{A}_{po}(E) \exp \left[\frac{i}{\hbar} S_{po}(E) - i\sigma_{po}\pi/2 - i\phi_d \right] \right\} . \end{aligned} \tag{11}$$

The sum is over all periodic orbits (isolated or families) (po) of the classical system (besides of the POs which belong to the same family on which the summation was already performed). $S_{po}(E) = \oint \mathbf{p} \cdot d\mathbf{r}$ are their action integrals, the amplitude $\mathcal{A}_{po}(E)$ (which in general is complex) is of the order of the phase space volume occupied by CT, and the factor given in Eq. (9) which depends on the degeneracies and stabilities of the POs, respectively. σ_{po} is called the Maslov index. ϕ_d is an extra phase that depends on the dimensionality of the system and degeneracy $\mathcal{K}$ of the PO manifold. (ϕ_d is zero when all orbits are isolated ($\mathcal{K}$=0), as defined in [13]). The sum in (11) is an asymptotic one, correct to leading order in $1/\hbar^{1/2}$, and in non-integrable systems it is hampered by convergence problems [13]. For systems in which all orbits are isolated in phase space, Gutzwiller [13] expressed the amplitudes $\mathcal{A}_{po}(E)$ (which are real in this case) explicitly in terms of the periods and stability matrices of the POs, see some examples below. His trace formula has become famous, in particular in connection with *"quantum chaos"* [13]. Notice that according to (9), any more exact integration in (3) over a bifurcation/catastrophe variable ξ of the improved SPM leads to an enhancement of the amplitude $\mathcal{A}_{po}$ in the form of a maximum in the transition interval from the bifurcation point to the region of the asymptotic (SSPM) behaviour of $\mathcal{A}_{po}$. The hight of this maximum is of order $1/\hbar^{1/2}$ as compared to the result of the standard SPM integration (integrable or non-integrable system; see more specific examples in Sects. 3.3 and 3.4).

The trace formula (11) thus relates the quantum oscillations in the level density to quantities that are determined purely by the classical system. Strutinsky, in his search for simple physical explanations of shell effects, realized that this kind of approach could help to understand the shell effects in terms of classical pictures. However, in the application to nuclear physics, Gutzwiller's expression for the amplitudes $\mathcal{A}_{po}(E)$ could not be used, because they diverge when the POs are not isolated in phase space. This happens whenever a system has continuous (e.g., rotational) symmetries, and hence for most typical shell-model potentials (except in non-axially deformed situations). Gutzwiller's theory was extended to systems with continuous symmetries in [15] (see also Chap. 6 of [4] for details).

Trace formulae for systems with all kinds of mixed symmetries, including the integrable cases, were also developed later by various other authors. The treatment of bifurcations is still an on-going subject of current research. Uniform approximations were constructed for orbit bifurcations and symmetry breaking under the variation of the energy or a potential parameter; references to most of these developments are given in [4], Chap. 6.

Strutinsky has, however, not only the merit of extending Gutzwiller's approach to realistic shell-model potentials, but he and his collaborators also extended the semiclassical approach to the description of bound many-fermion systems in the mean-field approach. In [15] it was shown that for such systems the shell-correction energy δE (2) (for one kind of particles) is given semiclassically by a similar-looking trace formula:

$$\delta E \simeq \delta E_{scl} = \mathrm{Re} \sum_{po} (\hbar/t_{po})^2 \mathcal{A}_{po}(E_F) \, \exp\left[\frac{i}{\hbar} S_{po}(E_F) - i\sigma_{po}\pi/2 - i\phi_d\right]. \tag{12}$$

The difference to the trace formula (11) for the level density is that here the amplitudes and actions are to be evaluated at the Fermi energy E_F of the considered particles, and the appearance of an extra factor $(\hbar/t_{po})^2$, where t_{po} are the times periods of the particle motion along the PO with M repetitions, $t_{po} = MT_{po}$, T_{po} being the primitive ($M = 1$) period of PO. This extra factor brings a natural convergence to the sum, different from that in (11): orbits with longer periods contribute less to the shell-correction energy (besides of amplitude enhancement of shell structure discussed above and further below). To obtain the energy shell correction δE (12) as function of the particle number N, one can use the standard relation of the Fermi energy E_F to the given particle number N,

$$N = 2 \int_0^{E_F} \mathrm{d}E \, g(E) \,. \tag{13}$$

The level density $g(E)$ can be approximated here with Eqs. (5) and (6) using the trace formula Eq.

(11) for its oscillating part.[1]

It is the beauty of this approach that gross-shell effects in δE often can be explained semiclassically in terms of a few of the shortest POs (with smallest periods) in the system. The earliest application of this idea by Strutinsky's group was given in [5], where the correct slopes of the stability valleys $\eta(N)$ of nuclei in a plot of δE versus particle number N and deformation η was correctly reproduced using the shortest orbits in a spheroidally deformed cavity at small η, as shown in Fig. 2. A further example will be given in Sect. 3.2. However, if one wants to study finer shell structures or some specific situations at large deformations, longer orbits have to be included. Hereby, bifurcations of POs can play a crucial role, as it will be exemplified in Sects. 3.3 and 3.4.

For billiard systems, it is advantageous to express the level density as a function not of energy E but of the wave number $k = \sqrt{2mE/\hbar^2}$, where m is the mass of the particle. By virtue of the simple k dependence of the phase function $S_{po}/\hbar$ in (11) for such systems through the product of wave number k and orbit length L_{po}, the Fourier transform of the level density $g(k)$ with respect to k yields directly its length spectrum and thus provides a nice tool to examine the quantum-classical correspondence. The Fourier transform of the semiclassical level density gives, indeed,

$$F(L) = \int g(k) e^{ikL} dk \simeq F_0(L) + \sum_{po} \widetilde{\mathcal{A}}_{po}\, \delta(L - L_{po}) \tag{14}$$

which has peaks exactly at the lengths of the periodic orbits $L = L_{po}$ with heights proportional to their amplitudes $\mathcal{A}_{po}$. $F_0(L)$ represents a Fourier transform of the smooth TF level density and has a peak at $L = 0$. Taking the Fourier transform of the exact quantum spectrum of the Hamiltonian thus reveals the classical periodic orbits, and the heights of the Fourier peaks give information about their semiclassical amplitudes.

It is often instructive to study a *coarse-grained level density* which is defined by convoluting the exact sum of delta functions in (3) with a normalized Gaussian function of finite width Γ:

$$g_\Gamma(E) = \frac{1}{\Gamma\sqrt{\pi}} \int_{-\infty}^{\infty} \mathrm{d}E' g(E') \, \exp[-(E - E')^2/\Gamma^2] = \frac{1}{\Gamma\sqrt{\pi}} \sum_n \exp[-(E - E_n)^2/\Gamma^2] \,. \tag{15}$$

Convoluting the semiclassical trace formula (11), one may expand the action $S_{po}(E')$ in the phases up to linear (and the amplitudes $\mathcal{A}_{po}(E')$ up to zero) order terms in $E' - E$, as long as Γ is small with respect to the distance between the gross shells near the Fermi surface, see [15]. In this way, one obtains the Gaussian-averaged trace formula

$$\delta g_{\Gamma,\mathrm{scl}}(E) = \sum_{po} \delta g_{po}^{\mathrm{scl}}(E) \, \exp\left\{ - \left(\frac{\Gamma t_{po}}{2\hbar} \right)^2 \right\} . \tag{16}$$

[1]For practical purposes, we use the coarse-grained expression defined in Eq. (17) below with a small value of γ to which E_F is quite insensitive.

For billiards, a corresponding Gaussian averaging with a width γ over the wave number k leads (with better accuracy owing to the linear dependence of the action on k) to the averaged trace formula

$$\delta g_{\gamma,\mathrm{scl}}(k) = \sum_{po} \delta g_{po}^{\mathrm{scl}}(k)\, \exp\left\{ -\left(\frac{\gamma L_{po}}{2}\right)^2 \right\}, \tag{17}$$

where L_{po} is the length of the PO, and the relation between the two smoothing widths is $\Gamma \simeq 2\gamma E/k$. We see that, depending on the smoothing width Γ (or γ), longer orbits are automatically suppressed in the above expressions and the PO sum converges – which it usually does not [13] for non-integrable systems in the limit Γ (or γ) $\to 0$. Thus, one can emphasize the *gross-shell structure* in the level density using a smoothing width which is much larger than the s.p. level spacing but smaller than the main shell spacing (the distance between gross shells) near the Fermi surface. Alternatively, finer shell structures can be studied using essentially smaller smoothing widths.

We note that the POT can also be applied to open systems above the continuum threshold, where the level density is dominated by resonances; an example has been given in [53]. As a first step towards dynamics, the oscillating parts of nuclear moments of inertia have been studied semiclassically in terms of POs in [54, 55].

Finally, we mention applications of the POT to finite fermion systems from other domains of physics such as mesoscopic semiconductor structures (e.g., quantum dots), metal clusters, and trapped fermionic atoms, described in [4] (Chapter 8) and [56, 57, 58, 59, 60].

3.2 SEMICLASSICAL CALCULATION OF A NUCLEAR FISSION BARRIER

One prominent feature in the fission of actinide nuclei (isotopes of U, Pu, etc.) is that their fragment distributions are asymmetric with a most probable ratio of fragment masses of ~ 1.3 - 1.5 (cf. [12]). This is an effect that cannot be described within the LDM which always favours the highest possible symmetries. It was one of the big successes of the SCM to explain the mass asymmetry of the fission fragments. The fragment distribution is, of course, a result of nuclear dynamics. However, already in static calculations of fission barriers, the onset of the mass (or left-right) asymmetry at the outer fission barrier was found in SCM calculations with realistic nuclear shell models [61, 62]. On the l.h.s. of Fig. 3, we show a schematic picture of the deformation energy of a typical actinide nucleus, plotted versus a suitably chosen deformation parameter (see below for a specific choice of deformations). The heavy dashed line is the average deformation energy obtained in the LDM; the thin lines are the results obtained when the shell-correction energy δE is included. They exhibit

the characteristic deformation effects of the shell structure in these nuclei: a deformed ground state and the characteristic double-humped fission barrier, split by a second minimum corresponding to the fission isomer. The solid line is obtained when only left-right symmetric deformations are used; the dashed thin line is obtained when one allows for left-right asymmetric shapes. As we see, the asymmetric shapes lower the outer fission barrier considerably. All shapes here are taken to be axially symmetric.

The mass asymmetry in nuclear fission was therefore understood as a quantum shell effect. In a detailed microscopical study [63] of the Lund group using the Nilsson model, it was shown that those single-particle states which are most sensitive to the left-right asymmetric deformations are pairs of states with opposite parity, having the nodes and extrema of their wave functions on parallel planes perpendicular to the symmetry axis at and near the waist-line of the fissioning nucleus, as shown on the r.h.s. of Fig. 3. Under the effect of the neck constriction one of these s.p. levels, which for actinides is just lying below the Fermi energy, is further lowered when the mass asymmetry is turned on. As a consequence, the asymmetry leads to a lowering of the total shell-correction energy and hence of the outer fission barrier, the LDM part of the energy being much less sensitive to the mass asymmetry. (As a historical note, we should emphasize that the essential role of such pairs of s.p. states for the mass asymmetry had already been recognized in 1962 by S.A.E. Johansson [30]. Unfortunately, at that time the SCM was not available and hence no realistic fission barriers could be calculated, as reported in Sect. 2.)

In this section, we want to show that the POT is able to reproduce this quantum shell effect, at least qualitatively, in s semiclassical description using the POT. We will focus here only on the gross-shell structure, like that seen in the qualitative picture of the fission barrier in Fig. 3.

The spheroidal cavity model used in [5] and discussed in Sect. 3.3 does not allow one to describe nuclear fission, since an ellipsoidal deformation is not sufficient to yield a finite barrier towards fission. In [26, 64, 65], a simple but more realistic "fission cavity model" was used. It consists of a cavity with the (c, h, α) shape parametrization that was used both for the LDM and for the deformed Woods-Saxon type shell-model potentials in the SCM calculations of [12]. These axially symmetric shapes are shown in Fig. 4. The parameter c describes the elongation of the nucleus (in units of the radius R_0 of a sphere containing $N = \rho_0 4\pi R_0^3/3$ particles, where ρ_0 is the bulk particle density), h is a necking parameter, and $\alpha \neq 0$ describes left-right asymmetric shapes shown by the dotted lines. The sequence of shapes with $h = \alpha = 0$ reproduces the optimized shapes of the LDM [33] (see [12] for details). Like in [5], spin-orbit and pairing interactions were neglected in [26, 64, 65] and, for simplicitly, only one kind of nucleons (without Coulomb interaction) was used. The only

parameter in the fission cavity model, the Fermi wave number $k_F = 12.1/R_0$, was adjusted to yield the second minimum at the deformation $h = \alpha = 0$, $c = 1.42$ which is that of the fission isomer obtained in [12] for the nucleus ^{240}Pu. This corresponds here to a particle number $N \simeq 180$, i.e., to $N^{1/3} \simeq 5.65$ when the spin-orbit interaction is neglected.

This procedure is justified by the observation that, to a first approximation, the spin-orbit and Coulomb interactions essentially lead to a shift of the magic numbers, preserving the relative shell structures in the energy shell-correction. This shift can be simulated by a shift of the Fermi energy as in [5]. The procedure works, however, only locally in a limited region of deformations and particle numbers. The results shown in Fig. 10 below suggest that it is successful in the region $1.3 \lesssim c \lesssim 1.65$; the ground-state deformations would, e.g., not be reproduced correctly with the same Fermi energy. [Note that, in principle, spin-orbit effects can be included in the POT [66, 67, 68] (see also [69] for a short overview). However, in non-integrable systems one is met with lots of bifurcations under the variation of the spin-orbit strength [70], which makes the POT with spin-orbit interactions very cumbersome. Similarly, the pairing interactions can also be included in the POT [71, 72], but this has not been done for nuclear deformations energies so far.]

In [26], the shortest POs in the (c, h, α) cavity were found to dominate the gross-shell features of the double-humped fission barrier. For the deformations around the barriers ($c \gtrsim 1.3$), the shortest POs are the primitive diagonal and regular polygonal orbits in planes perpendicular to the nuclear symmetry axis, situated at the extrema of the cavity shape function (see the l.h.s. of Fig. 8 below). At the onset of the neck ($c = 1.49$ for $h = \alpha = 0$), the orbits in the central equatorial plane become unstable with respect to small perturbations perpendicular to the equatorial plane and give birth to new stable orbits lying in planes parallel to the equatorial plane. In the restricted deformation space with $\alpha = 0$, these bifurcations are of pitchfork type; they are isochronous due to the reflection symmetry with respect to the equatorial plane (cf. [73], Sect. II.B.2, for a discussion of this generic bifurcation type). When the asymmetry $\alpha \neq 0$ is turned on in the presence of a neck, the bifurcation is of a more complicated type. These bifurcations were treated in a uniform approximation employing a suitable normal form for the action function (see [26] for details). (Note that with respect to small perturbations within the equatorial plane, all these orbits are marginally stable, forming degenerate families with degeneracy $\mathcal{K} = 1$ due to the axial symmetry of the cavity.)

Before summarizing the results of [26], let us study the general trends of the shell effects obtained in the fisson cavity model and try to understand them in terms of the leading POs.

In Fig. 5 we show a contour plot of the quantum-mechanical shell-correction energy δE calculated from the s.p. energy spectrum of the fission cavity model, shown versus the cube-root of the particle

number $N^{1/3}$ and the elongation parameter c along $h = \alpha = 0$ (white: positive values, gray to black: negative values). The horizontal dotted line for $N \simeq 180$ (i.e., $k_F = 12.1/R_0$) corresponds to the situation where the isomer minimum lies at $c \simeq 1.4$ and the outer (symmetric) barrier is peaked around $c \simeq 1.55$, as seen in Figs. 7 - 10 below. The heavy lines give the loci of constant actions of the leading POs (3,1,1)s: meridional triangles; (2,1)EQ: equatorial diameters; (2,1)AQ: diameter orbits in planes parallel to the equator plane. We see that these lines follow the valleys of minimal shell-correction energy. For the valleys corresponding to the ground-state deformations, the situation is like in Figs. 2 (Sect. 1) and 23 (Sect. 3.3 below) obtained for the spheroidal models, but here for the more realistic fission cavity model; in all cases the meridional orbits dominate the ground-state valleys. The valleys corresponding to the fission isomers, starting around $c \sim 1.3$, are determined by the shortest POs in the planes perpendicular to the symmetry axis: up to $c \sim 1.5$, these are the equatorial orbits EQ; after their bifurcation at $c = 1.49$, the valleys are seen to curve down towards smaller values of $N^{1/3}$, following the constant-action lines of the stable POs in the planes parallel to the equator plane (dashed lines, AQ) which have larger semiclassical amplitudes than the equatorial orbits (EQ) that for $c > 1.49$ have become unstable. The fact that the quantum-mechanically obtained stability valleys follow the (dashed) lines AQ after their branching from the lines EQ is a remarkable quantum signature of the classical bifurcation effect.

The most striking feature of the gross-shell structure seen in Fig. 5, namely the opposite slopes of the ground-state valleys ($1 \lesssim c \lesssim 1.25$) and the isomer valleys ($c \gtrsim 1.3$), are thus understood semiclassically in terms of the opposite deformation dependence of the dominating meridional POs in the former valleys and the POs in planes perpendicular to the symmetry axis in the latter valleys, respectively.

These results can be further elucidated by looking at the Fourier spectra in Fig. 6 for the five values (from top to bottom) $c = 1.1$, 1.2, 1.4, 1.5, and 1.6 (all for symmetric shapes with $h = \alpha = 0$). The short arrows underneath the Fourier peaks indicate the lengths of the equatorial orbits: diameter (2,1)EQ and its second repetition 2(2,1)EQ, triangle (3,1)EQ, etc., and (for $c = 1.6$) the corresponding orbits AQ in the planes parallel to the equator plane. The long arrows correspond to the meridional orbits: triangle (3,1,1)s and quadrangle (4,1,1)s. We see that for the small deformations $c = 1.1$ and 1.2, the meridional orbits have the strongest amplitudes and hence dominate the shell structure in yielding the ground-state deformation valleys seen in Fig. 5. The equatorial orbits EQ and their bifurcated partners AQ have the largest amplitudes for $c = 1.4 - 1.6$, which explains their dominance in yielding the isomer valleys.

Since the trace formula (12) for the shell-correction energy δE contains the squares $(\hbar/t_{po})^2$ of

the inverse periods of the POs, apart from the amplitudes $\mathcal{A}_{po}$ of the semiclassical level density (11), there is a natural suppression of longer orbits contributing to δE. This ensures the convergence of the PO sum, particularly in non-integrable systems (like the one considered here) where the PO sum for the level density (11) usually does not converge [13]. This suppression is particularly effective amongst orbits with comparable amplitudes $\mathcal{A}_{po}$. It explains why already at $c = 1.4$, where the meridional orbits (3,1,1)s and (4,1,1)s still have similar amplitudes as the EQ orbits,[2] the latter dominate the shell structure (by a factor ~ 4 in case of the EQ2 orbit), as suggested by Fig. 5.

In Fig. 6 we have marked some of the peaks around $7 \lesssim L \lesssim 8.5$ for $c = 1.4$ and around $6.5 \lesssim L \lesssim 8$ for $c = 1.5$ and 1.6. They correspond to orbits born from the equatorial orbits in period-doubling bifurcations; some of them are 3-dimensional orbits. Similarly, there are many other peaks at $L \gtrsim 8$, some of which correspond to orbits born in higher m-tupling ($m \geq 3$) bifurcations. The contributions of all these orbits to the gross-shell structure is, however, practically negligible due to their long periods. They have therefore not been included in the results presented below. They might, however, become noticeable in POT calculations with higher resolution of the shell structure (see the discussions in Sects. 3.3 and 4).

We should also recall the fact that in realistic SCM calculations, the pairing interactions are known to reduce the amplitude of δE by up to $\sim 30\%$ (see, e.g., [12]). In the POT, the pairing effects [71, 72] yield, indeed, an extra smoothing factor in the semiclassical amplitudes, which further suppresses the contributions of longer orbits.

Fig. 7 shows a comparison of the level density in the fission cavity model, taken at the Fermi wave number $k_F = 12.1/R_0$ and plotted versus c along $h = \alpha = 0$ in the region covering the isomer minimum and the outer fission barrier. [As noted above, the model without spin-orbit interaction and one fixed Fermi energy does not work at all deformations. For this reason the deformations $c < 1.25$ are not shown.] The solid line is the quantum-mechanical result and the dashed line the result of the semiclassical trace formula (with uniform approximation [26] for the bifurcation at $c = 1.49$) including all primitive POs with up to 20 reflections at the boundary in the planes perpendicular to the symmetry axis. Both results have been coarse-grained by a Gaussian averaging over the wave number k with a width $\gamma = 0.6/R_0$ that emphasizes the gross-shell structure. We see that the agreement is nearly perfect. This figure also demonstrates that already a very simple cavity model with one degree of freedom (c, keeping $h = \alpha = 0$ fixed) is capable of yielding the

[2]The strong Fourier peak near $L/R_0 \sim 6.3$ for $c = 1.4$ in Fig. 6 contains the combined amplitudes of the meridional quadrangle (4,1,1)s and the second repetition of the equatorial diameter orbit, 2(2,1)EQ. Although the two cannot be disentangled, we estimate that both these orbits have comparable amplitudes.

main features of the double-humped fission barrier.

Let us now look at the influence of left-right asymmetric shapes with $\alpha \neq 0$ on the shell-correction energy and, in particular, on the height of the second fission barrier. In Fig. 8, the semiclassical result of δE is shown in a perspective view as a function of elongation c and left-right asymmetry α, taken along $h = 0$ in the region of the isomer minimum and the outer fission barrier. We see how the outer fission barrier is lowered for left-right asymmetric shapes. Instead of the heigher barrier obtained for left-right symmetric shapes with $\alpha = 0$ (arrow labeled "symm."), the nucleus can go towards fission over a lower saddle when asymmetric shapes are allowed (arrow labeled "asymm."). To the left, we see the shapes corresponding to the three points A (fission isomer), B and C (along the asymmetric fission path) in the deformation energy surface. The vertical lines indicate the planes in which the POs are situated (solid lines for stable and dashed line for unstable POs).

The instability of the outer fission barrier towards left-right asymmetric deformations, known from the quantum-mechanical SCM calculations [61, 62], can thus be described semiclassically using the POT, indeed. Hereby only the shortest primitive POs are relevant due to the fast convergence of the PO sum for the semiclassical shell-correction energy δE, as discussed above.

This convergence is also demonstrated in Fig. 9. It shows the Fourier transform of the level density obtained for the asymmetric shape with c=1.5, h=0, α=0.12, corresponding to the point B shown in Figs. 8 and 10 below, coarse-grained as in Fig. 7. The insert depicts the corresponding shape. The solid line is the quantum-mechanical and the dashed line the semiclassical result; the two are seen to agree very well. We notice that the most significant peaks correspond to the lengths L/R_0 of the primitive orbits $(p, 1)$AQ with $p = 2$, 3, 4, and 5 reflections. Some of the small peaks at $L > 6R_0$ correspond to their second repetitions, the other come from meridional orbits. These do, however, not affect the gross-shell structure (cf. also Fig. 4 in [64]).

In Fig. 10, we compare the old quantum-mechanical results of SCM calculations [12] with realistic deformed Woods-Saxon potentials [11] with the semiclassical POT results using the present simple fission cavity model. Shown are contour plots of δE versus c and α for two values of the neck parameter h. We see that the semiclassical results (r.h.s.) reproduce the gross-shell structure of the quantum results (l.h.s.) very well. The correct topology is obtained, displaying the lowering of the outer barrier for left-right asymmetric shapes. Also, the amplitudes of the shell effects on both sides are comparable, which justifies our calculating only the gross-shell structure using the shortest periods on the semiclassical level. Of course, a detailed quantitative agreement cannot be expected for the two calculations using such different potentials as the sophisticated smooth Woods-Saxon potential including pairing, spin-orbit, and Coulomb interactions on one side (left), and the

simple fission cavity model without these extra interactions on the other side (right). The more gratifying is the good overall good qualitative agreement of the gross-shell structure. This agreement demonstrates, by the way, an experience made from quantum-mechanical SCM calculations using realistic nuclear shell model potentials: the gross-shell features of the fission barriers are much less sensitive to the radial dependence of the potentials than to its deformation. Hence the success of a simple cavity model that is very schematic, but uses the realistic c, h, α deformations.

The white dashed lines in the r.h.s. panels of Fig. 10 show the loci of constant classical actions $S_{\rm PO}$ of the leading POs. They follow exactly the valleys of minimal energy in the (c, α) planes which define the adiabatic fission paths. Thus, as it was already observed in [5] and seen in Fig. 5, the condition for minimizing the shell-correction energy is semiclassically given by a least-action principle: $\delta S_{\rm PO} = 0$.

We should emphasize that in Figs. 8 and 10 only the shell-correction energy δE is shown. The complete fission barrier is obtained by adding its smooth LDM part, according to (1), which for ^{240}Pu in the (c, h, α) parametrization occurs [12] at $c \simeq 1.45 - 1.5$, $h = \alpha = 0$. Since the LDM barrier is rather smooth around its maximum, the relative heights of the isomer minimum and the outer barrier are not affected much by it. However, for $c \gtrsim 1.6$ the LDM barrier is already going steeply down. Therefore in the total energy, the minimum around $c \simeq 1.65 - 1.7$ seen in Figs. 8 and 10 along $h = 0 = \alpha = 0$ (like also in Fig. 7) vanishes in the steep slope of the total fission barrier, as shown schematically in Fig. 3.

It is also interesting to note, as demonstrated explicitly in [65], that the quantum-mechanical probability maxima of those s.p. states which microscopically are responsible [63] for the asymmetry effect in the SCM approach (see the schematic plot on the r.h.s. of Fig. 3) lie exactly in the planes perpendicular to the symmetry axis that contain the classical POs. This constitutes a nice quantum-to-classical relationship. It was also shown in [65] that the classical dynamics of the nucleons with small angular momenta L_z is more than 90% chaotic in the region of the outer barrier. A very small phase-space region of regular motion is thus sufficient to create the shell effect that leads towards the asymmetric fission of the nucleus!

We emphasize once more that the fission cavity model, in its present form without spin-orbit and Coulomb interactions, is not suitable for predicting fission barriers for a larger range of nuclear isotopes and deformations. The present semiclassical calculation should be taken as a model study of a typical actinide fission barrier, demonstrating that the POT in principle is capable of explaining the existence of a double-humped barrier, and also the onset of mass asymmetry around the outer barrier, in terms of a few short classical periodic orbits. It was in no way meant as a substitute

for the quantum-mechanical SCM for calculations of static fission barriers. Its aim was rather to provide, as suggested by the late Strutinsky, a qualitative physical understanding of a sophisticated quantum shell effect by means of simple classical pictures.

3.3 SPHEROIDAL CAVITY

As one of the main subjects in this report, we apply the semiclassical theory to a 3D spheroidal (prolate) cavity [5, 19, 20], which may be taken as a simple model for a large deformed nucleus or a (highly idealized) deformed metallic cluster [4]. We shall investigate the role of orbit bifurcations in the shell structure in connection with the superdeformation (corresponding to the fission isomer of heavy nuclei). Although the spheroidal cavity is integrable, it exhibits all the difficulties mentioned above (i.e., bifurcations and symmetry breaking) and therefore gives rise to an exemplary case study of a nontrivial 3D system. We apply the ISPM (see sect. 3.1) for the bifurcating orbits and succeed in reproducing the superdeformed shell structure by the POT, hereby observing a considerable enhancement of the oscillation amplitudes of the level density and the energy shell corrections near the bifurcation points and for larger deformations.

3.3.1 *CLASSICAL DYNAMICS*

We consider a cavity system having a spheroidal shape boundary with the lengths of minor and major axis a and b, respectively, with a conserved volume $a^2 b = R^3$. The spheroidal deformation is therefore described by a single parameter, which we take to be the axis ratio $\eta = b/a$. The classical dynamics of particles in the spheroidal cavity can be solved in terms of action-angle variables related to the elliptic coordinates $\kappa = v, u, \varphi$ in this Hamiltonian system. The Hamiltonian, $H(I_v, I_u, I_\varphi)$, depends only on the partial actions [5, 20],

$$\begin{aligned} I_v &\propto \int_{v_{min}}^{v_{max}} \mathrm{d}v \sqrt{\cosh^2 v - I_1 - I_2/\sinh^2 v}\,, \\ I_u &\propto \int_{-u_{max}}^{u_{max}} \mathrm{d}u \sqrt{I_1 - \sin^2 u - I_2/\cos^2 u}\,, \qquad I_\varphi \propto \sqrt{I_2}\,, \end{aligned} \tag{18}$$

where I_1 and I_2 are new single-valued separation constants, introduced for convenience instead of the two remaining free actions for the fixed energy by using the energy conservation of the particle motion: $E = H(I_u, I_v, I_\varphi)$, and the boundaries of the spatial part of the phase-space occupied by classical trajectories are shown explicitly in the integration limits. (These two constants are identical to σ_1 and σ_2 in the notation of Refs. [5, 20]). The periodic-orbit (SPM) equations (7) for the stationary points I_1^* and I_2^* can be written as a resonance condition of commensurability of the

partial frequencies:

$$\omega_v : \omega_u : \omega_\varphi = n_v : n_u : n_\varphi \ , \qquad \text{with} \qquad \omega_\kappa = \partial H / \partial I_\kappa \ . \tag{19}$$

For definiteness, we shall consider only prolate spheroidal deformations, $\eta > 1$, following the suggestions in [5].

The POs in the spheroidal cavity can be classified as follows: a) meridional (elliptic, 2DE) orbits, denoted by $M\,(n_v, n_u)$ ($n_v \geq 2n_u$), and b) equatorial (EQ) orbits, denoted by $M\,(n_v, n_\varphi)$ ($n_v \geq 2n_\varphi$). Hereby M is the repetition number of the primitive orbits which are characterized by the positive integers n_v = number of corners and n_u, n_φ = winding numbers), see Figs. 11 and 12, respectively. Both these types of orbits exist at all deformations $\eta > 1$. c) There are also specific families of orbits which exist only at specific deformations larger the critical (bifurcation) value, $\eta > \eta_{bif}$, where they are born from the EQ POs in pitchfork-like bifurcations. Examples of such bifurcated orbits $M(n_v, n_u, n_\varphi)$ are the meridional hyperbolic orbits (2DH), e.g., the butterfly (4,2,1) (see the fourth orbit in Fig. 11), which bifurcates from the doubly repeated EQ diameter 2(2,1) (cf. the first orbit in Fig. 12) at the deformation $\eta_{bif} = \sqrt{2}$ and exists for all deformations $\eta > \sqrt{2}$ along with the diameter 2(2,1). Another important example is the bifurcation of the equatorial star orbit (fourth orbit in Fig. 12) at $\eta = 1.618...$ where the new 3D orbits (5,2,1) emerge from the parent orbit (see the first orbit in Fig. 13); again both exist at all larger deformations. One also finds a bifurcation of the doubly repeated EQ triangle 2(3,1) which bifurcates at $\eta = 1.732$, whereby the new 3D orbits (6,2,1) emerge.

For the following it is useful to note the classical degeneracies $\mathcal{K}$ of the above-mentioned POs [15, 18, 20, 21]. The meridional (planar) orbits (denoted by "2D" henceforth for both elliptic 2DE and hyperbolic 2DH POs) and all 3D orbits have the degeneracy $\mathcal{K} = 2$, so that the largest phase-space volume is covered by these PO families. The POs in the equatorial plane (denoted by "EQ") have the degeneracy $\mathcal{K} = 1$ (except at the critical bifurcation points where they are degenerate with the newborn orbit families having $\mathcal{K} = 2$). There is also an isolated ($\mathcal{K} = 0$) diametric orbit along the symmetry axis for $\eta > 1$, but its contribution can be neglected for sufficiently large deformations as compared to all other orbits.

In the following subsections, we will show more explicitly that bifurcations of POs are not just a technical obstacle which appears in the semiclassical POT, but that they leave signatures in the quantum-mechanical results of the system and thus cause physical phenomena like in Sect. 3.2.

3.3.2 *TRACE FORMULAE AND SHELL STRUCTURE ENHANCEMENT*

The contributions of the above periodic orbits are in the following separately considered according to their degeneracies $\mathcal{K}$ discussed above. According to Eq. (11), the oscillating part of the level density is thus given semiclassically by

$$\delta g_{\rm scl}(E) = \delta g^{(2)}_{\rm 3D}(E) + \delta g^{(2)}_{\rm 2D}(E) + \delta g^{(1)}_{\rm EQ}(E), \tag{20}$$

$$\delta g^{(\mathcal{K})}(E) = {\rm Re} \sum_{po} \mathcal{A}^{(\mathcal{K})}_{po} \exp\left(ikL_{po} - i\frac{\pi}{2}\sigma^{(\mathcal{K})}_{po} - i\phi^{(\mathcal{K})}_{d} \right). \tag{21}$$

For the explicit analytical expressions of the amplitudes $\mathcal{A}^{(\mathcal{K})}_{\rm po}$, constant phases $\sigma^{(\mathcal{K})}_{po}$ and $\phi^{(\mathcal{K})}_{d}$, see Ref. [20].

Figs. 14 and 15 show the characteristic enhancement of the semiclassical amplitudes near the bifurcations of the EQ orbits (5,2) and 2(3,1), respectively. As clearly seen from these Figures, the ISPM amplitude (solid lines) $\mathcal{A}_{EQ}$ has a pronounced but finite maximum instead of the divergence of the SSPM amplitude (dashed lines) at the corresponding critical points 1.618... and 1.732... . The SSPM amplitudes $\mathcal{A}_{3D}$ for the bifurcated 3D families (5,2,1) and (6,2,1) have discontinuities at these deformations. Their ISPM amplitudes are continuous curves with an enhancement in the form of a rather wide maximum slightly to the right of the critical deformations. The relative enhancement near the bifurcations is of order $\hbar^{-1/2}$ [or $(k_F L_{po})^{1/2}$ at the Fermi energy $E = E_F$]. As noted in sect. 3.1, it is due to one more exact integration in the improved SPM, as compared to the standard SPM. This enhancement occurs around the critical deformation (on both sides) for the parent orbits and to the right of the bifurcation point for the newborn POs. For any integrable and non-integrable systems, one has an increase of the classical degeneracy of the parent orbits locally at the bifurcation point. The newborn POs form families having the larger degeneracy ($\mathcal{K} = 2$) at the critical point and all larger deformations, as noted above. This discrete behavior of the classical degeneracies is "smeared out" semiclassically in the ISPM over the regions around the bifurcation point (or slightly on its right) where the enhancement is found in the amplitudes of Figs. 14 and 15 for the general reasons discussed in Sect. 3.1.

We observe also some smaller oscillations in these amplitudes further away from the bifurcation points. They can be neglected with respect to the enhancement at the order of the semiclassical parameter discussed above. In any case, to improve the SPM with respect to its standard version (SSPM), we have to use finite limits in the integration over a phase-space volume occupied by CT trajectories as given in the *more exact* expression (3) for the level density (before applying further approximations to the trace of the semiclassical Green function).

Within the simplest ISPM, using the expansion of the action phase near the stationary point up

to second-order terms like in (9) ("2nd-order ISPM"), one can extend the integration limits to $\pm\infty$ for deformations asymptotically far from the bifurcations in order to obtain the SSPM asymptotics. For more exact higher-order expansions of the action (8), for example up to third-order terms ("3rd-order ISPM"), the convergence for the extension of the integration limits to an infinite region can be sufficiently good, even near the bifurcations, see [20]. As shown from the comparison of the 2nd and 3rd order ISPM approaches in Figs. 11 and 12 in [20], the convergence of this expansion around the bifurcation points is rather fast and, therefore, it can be stopped at the 2nd order ISPM, but with finite limits.

3.3.3 *COMPARISON WITH QUANTUM RESULTS*

We now compare numerically our semiclassical results for the spheroidal cavity with exact quantum-mechanical results. In Figs. 16 and 17 we show the oscillating part of the level density $\delta g_\gamma(k)$ versus the wave number k for six charecteristic values of the deformation parameter η. Both the quantum-mechanical (solid lines) and the semiclassical (dotted lines) level densities have been averaged over a Gaussian width of $\gamma = 0.3/R$, in order to emphasize some finer shell structure besides the gross-shell oscillations. In Figs. 18 and 19 we show the results for the energy shell-correction δE. The quantum results (solid lines) are obtained by the shell-correction method, see (2), from the quantum spectrum of the spheroidal cavity. The semiclassical results are obtained using (12) which, in analogy to (20), becomes

$$\delta E_{scl} = \mathrm{Re} \sum_{\mathcal{K},po} \left(\frac{\hbar}{t_{po}}\right)^2 \mathcal{A}_{po}^{(\mathcal{K})}(E_F) \exp\left(ik_F L_{po} - i\frac{\pi}{2}\sigma_{po}^{(\mathcal{K})} - i\phi_d^{(\mathcal{K})}\right), \tag{22}$$

where the sum is over the same three orbit families as in (20) and $t_{po} = mL_{po}/p_F$ are their periods, taken at the Fermi momentum $p_F = \hbar k_F = \sqrt{2mE_F}$ which is fixed for each particle number N through (13).

A close examination of contributions of individual POs at the deformation $\eta = 1.2$, see Figs. 16 and 18, shows that a good agreement between the semiclassical (ISPM or SSPM) and quantum calculations is obtained by including only short (period-one) elliptic 2D (2DE) and EQ orbits. More specifically, we find a rather good convergence of the PO sums by using the 2DE orbits with $n_v \leq 12$, $n_u = 1$ and the EQ orbits with maximum vertex and winding numbers $Mn_v = 14$ and $Mn_\varphi = 1$, respectively. For small and medium deformations up to $\eta \simeq 1.4$, one has a clear dominance of the gross-shell structure by the shortest meridian and equatorial POs, similar to the situation in the fission cavity model (see Fig. 5) up to $c \simeq 1.4$ (see also the discussion below in connection with Figs. 21 and 23).

At $\eta = \sqrt{2}$, there occurs a bifurcation of the doubly repeated EQ diameter 2(2,1) with the emer-

gence of the butterfly orbits (4,2,1)2DH, and the improved SPM becomes important in comparison with the quantum results, see the second panels of these figures. However, even at these deformations ($\eta \lesssim 1.4$), as shown in [20], these longer orbits do not influence much the gross-shell structure due to the leading period-one orbits mentioned above. Noticeable ISPM contributions of the bifurcating (4,2,1)2DH orbits are found in the lowest panels of Figs. 16 and 18 for $\eta = 1.5$, in agreement with the enhancement of their amplitudes to the right of their bifurcation point. At $\eta = 1.5$, these contributions become comparable in magnitude with respect to those of the period-one orbits, although they have similar periods, and they become even larger with increasing deformation and particle number. Thus, for $\eta \gtrsim 1.5$ one has a transition from period-one to period-two dominating PO contributions; the latter are strongest at $\eta = 2$ and beyond.

Figs. 17 and 19 show the cases of superdeformed states exactly at the bifurcation points $\eta =$ 1.618..., 1.732... and 2.0. The quantum results are here nicely reproduced by the semiclassical ISPM results (like for $\eta = 1.414...$ above) including the dominant contributions from the bifurcating orbits. Their important role is illustrated in Fig. 20 for the same superdeformations $\eta \gtrsim 1.6$, where only a few bifurcated period-two orbits are used in the ISPM results, which are again compared to the quantum results. It is seen from this Figure that the main features (periods and amplitudes) of the shell and supershell structures are in fairly good agreement which becomes the better the larger particle number. Some of the remaining discrepancies are still due to the (much smaller) contributions of period-one orbits and some other missing period-two orbits.

The importance of the bifurcating period-two orbits at these larger deformations is further stressed in the following two figures. In Fig. 21, the thin solid and dotted lines are again the quantum and semiclassical ISPM results, like in Figs. 18, 19 and 20, showing a good agreement. The heavy line shows the ISMP result which is obtained if one uses only the shortest (period-one) orbits. We see that with increasing values of η and $N^{1/3}$, the resulting gross-shell structure does not reproduce the basic features mentioned above. At the superdeformation $\eta = 2$, the shortest alone orbits fail, in fact, completely to reproduce the gross-shell structure. At $\eta = 1.732...$, the shell structure is dominated mainly by the (4,2,1)2DH and (5,2,1)3D orbits, which have emerged from bifurcations at $\eta_{bif} = 1.414...$ and 1.618..., respectively, and by the 2(3,1)EQ and (6,2,1)3D orbits bifurcating exactly at $\eta_{bif} = 1.732....$ At $\eta_{bif} = 2$, the (6,2,1)2DH orbits bifurcate from the 3(2,1)EQ orbits. Besides these and the above-mentioned POs, also other new bifurcating period-three orbits like (7,3,1) and (8,3,1) 3D – besides the 3(2,1)EQ orbits which have enhanced amplitudes at $\eta = 2$ as usually – are determining the semiclassical shell-correction energies.

These findings are also transparently supported in Fig. 22 by the quantum Fourier spectra at the

same deformations as above (see a more detailed discussion of the Fourier spectra below). Many high peaks in the superdeformed region $\eta = 1.6 - 2.0$ remarkably confirm that the period-two POs are mainly responsible for the shell structure here and dominating above the period-one POs, especially clearly so at $\eta \sim 1.7 - 2.0$.

We see, therefore, that in the superdeformed region, the period-one orbits alone cannot explain the shell structure. The reason why the bifurcated period-two orbits become so important lies in their enhanced semiclassical amplitudes (cf. Figs. 14 and 15 above) which significantly overcome the suppression due to the $1/L_{po}^2$ factor in (22). One important ingredient of this enhancement is the larger phase-space volume covered by the newborn orbits due to their degeneracy $\mathcal{K} = 2$ (see Sect. 3.1 for a more general discussion of the origins of the enhancement).

In Figs. 23 and 24 we plot the quantum-mechanical shell-correction energy δE as function of deformation η and particle number $N^{1/3}$ in order to study its shell structure. The basic gross-shell structure of the energy valleys of minima is nicely described by the constant-action curves of the leading shortest POs at deformations smaller than the superdeformed shapes, as shown in Fig. 23. The main features are rather similar to those seen in Fig. 2 for the Woods-Saxon potential with spheroidal shapes, taken from [5], and also similar to Fig. 5 for relatively small deformations in the more realistic fission cavity model. In the region of small deformations, the dominant period-one orbits are the meridional 2DE orbits (3,1,1) and (4,1,1) whose constant-action lines follow precisely the down-going ground-state valleys in all three models. At larger intermediate deformations $1.3 \lesssim \eta \lesssim 1.5$, the slopes of the upgoing second-minimum valleys are roughly followed by the constant-action lines of the period-one orbits (2,1)EQ and (3,1)EQ, which is similar again as in Fig. 5 for the fission cavity model for $1.25 \lesssim c \lesssim 1.5$. However, for $\eta \gtrsim 1.6$ the secondary minimum valleys have a trend to bend down towards smaller values of $N^{1/3}$ with increasing η ,[3] which is not explained by the primitive EQ orbits. This trend can only be explained by the influence of the longer orbits which bifurcate from the higher repetitions of the EQ orbits. As seen from Fig. 24, the constant-action lines of the newborn orbits (4,2,1), (5,2,1) and (6,2,1) do, in fact, follow the downbending of the second-minimum valleys very nicely, especially for $\eta \gtrsim 1.7$ in good agreement with Fourier peaks in Fig. 22. In the region where the downbending begins, $\eta = 1.4 - 1.5$, the dominance of the 2(2,1)EQ and the newborn 2DH orbits born at $\eta_{bif} = \sqrt{2}$ reflects the enhancement of their semiclassical amplitudes at and beyond the critical deformation. This confirms the conclusions drawn above in connection with Figs. 21 and 22. In the region of superdeformations $\eta \gtrsim 1.6$, the newborn period-two and period-three orbits dominate the gross-

[3]Note that this trend can also be seen in Fig. 2 for the diffuse Woods-Saxon potential with spheroidal deformations.

shell structure of the shortest (period-one) EQ orbits completely, as clearly seen also from Fig. 22.

[Note that similar properties of the superdeformed shell structure owing to the amplitude enhancement of the dominating bifurcated period-two (and higher period) orbits were shown in more detail, including the comparison of the maps of the energy shell corrections $\delta E(\eta, N)$ for quantum and semiclassical calculations (with and without bifurcating POs), in Fig. 20 of [18]. In particular, the ISPM results for δE were in nice agreement with the quantum results at all critical characteristic deformations. The bifurcating period-two orbits were important to reproduce the superdeformed shell structure at $\eta \gtrsim 1.6$ like for the present spheroid cavity.]

We point out that the type of the bifurcations causing the downbending of the isomer valleys in the fission cavity model, seen in Fig. 5, is a different one: there it is the period-one bifurcation of the primitive EQ orbits at $c = 1.49$ which gives birth to the AQ orbits (also of period one) whose constant-action lines follow correctly the downbending for $c \gtrsim 1.5$. It is a subject of our ongoing research to investigate how bifurcations of further period-one and period-two orbits in the fission cavity model will affect finer details of the shell structure and, in particular, the "quantization" of the various local minima along the isomer valleys (see also the discussion in Sect. 4).

Note that in the axially-symmetric deformed 3D harmonic oscillator, discussed in [5], a smooth upgoing behaviour of the valley of minimal δE is more pronounced due to the shortest EQ orbits along their constant-action lines (following the gross-shell structure). It is accompanied by deeper local minima along the valleys (see Fig. 2d in [5]). They are associated with the amplitude enhancement owing to the longer-3D orbit bifurcations causing finer shell structure details. These local minima are related to the bifurcations of the simplest 3D orbits, for instance (3,2) at the deformation $\eta = \omega_\perp/\omega_z = 1.5$ and (2,1) at 2.0, where $\omega_\perp$ and ω_z are the HO frequencies perpendicular and parallel to the symmetry axis. The bifurcation amplitude enhancement near the intermediate deformation $\eta \approx 1.5$ there does not destroy the leading gross-shell structure valleys, like in the two cavity models discussed here. However, the decreasing slopes at superdeformations $\eta \approx 2$ are much less pronounced in the deformed HO model. We emphasize the important difference of the cavity models with respect to the deformed HO that the enhancement of the amplitudes of the bifurcating orbits occurs for all deformations larger than the bifurcation point, see [5]. We may also point out that the downgoing ground-state deformation valleys, due to the meridional orbits in the present cavity models, are absent in the harmonic oscillator and, in fact, degenerated into one spherical point $\eta = 1$. Each of the bifurcating 3D orbits appears and exists only at one deformation in the HO, whereas they exist in both cavity models at all deformations larger than their bifurcation

points.

The above discussed properties of the gross and fine shell structure related to the shortest and the bifurcating period-two orbits in the spheroidal cavity are nicely confirmed also by Fig. 25, where we show the modulus of the Fourier transform $|F(L)|$, see Eq. (14), of the quantum spectrum of the spheroidal cavity, plotted versus the orbit-length variable L and deformation η. It exhibits clear quantum signatures of the amplitude enhancement owing to the newborn orbits above their bifurcation points (marked by black dots). Besides the enhancement of $|F(L)|$ at the PO lengths (3,1), (4,1) (and others) at the spherical shape ($\eta = 1$), we observe the enhancement also above the bifurcation of the butterfly orbit at $\eta = \sqrt{2}$ and the superdeformations 1.618..., $\sqrt{3} = 1.732...$ etc., with the specific PO lengths $L = L_{(5,2,1)}$, $L_{6,2,1)}$, etc. The enhanced Fourier signals, which correspond to the highest peaks in Fig. 22, follow precisely the various lines in Fig. 25 which show the lengths of the classical POs (as explained in the insert on the upper right). This is again a nice quantum-to-classical correspondence, showing that classical periodic orbits and their bifurcations do have a physical relevance in the quantum spectrum of this system.

It is worth noting that the semiclassical origins of the deformed shell structures discussed above are related with bridge orbits [56], at least for potentials with finite diffuseness which can be approximately described by the power-law potential discussed in the following subsection. In a power-law potential with spheroidal shape, we have strong enhancement of shell effects due to the bridge orbit bifurcation ($n : m$) which emerges from a period-n-tupling bifurcation of equatorial orbits and submerges into a symmetry-axis orbit through a period-m-tupling bifurcation, forming the "bridge" between those POs, (see [56] for details). The meridional 2DE orbits $(n, 1, 1)$ responsible for the deformed shell structure at small deformations correspond to (1:1) bridges, and the meridional 2DH and 3D orbits $(n, 2, 1)$ responsible for the superdeformed shell structures correspond to (2:1) bridges, and so on. In the next subsection, we discuss the power-law potential with spherical shape, which also shows bifurcation enhancement effects at certain values of the diffuseness parameter.

3.4 RADIAL POWER-LAW POTENTIALS

The idea of [28] is that the spherical Woods-Saxon (WS) potential, known as a realistic mean-field potential model for spherical nuclei and metallic clusters, is nicely approximated (up to a constant shift and without the spin-orbit term) by much a simpler power-law potential[4] which is proportional

[4]Note: The potential power parameter α here should not be confused with the asymmetry deformation parameter of Sect. 3.2.

to a power of the radial coordinate r^α

$$V(r) = U(r/R)^\alpha. \tag{23}$$

With a suitable choice of the parameters U and α, the approximate equality

$$V_{WS}(r) \approx V_{WS}(0) + U(r/R)^\alpha$$

holds up to $r \lesssim R$, where $R = r_0 A^{1/3}$ with $r_0 = 1.2$ fm represents the nuclear radius for a given mass number A. Thus one finds nice agreement of the quantum spectra up to Fermi energy.

The potential (23) includes the limits of the harmonic oscillator ($\alpha = 2$) and the cavity ($\alpha \to \infty$); realistic nuclear potentials with steep but smooth surfaces correspond to values in the range $2 < \alpha < \infty$. The advantage of this potential is that it is a homogeneous function of the coordinates, so that the classical equations of motion are invariant under the scale transformations:

$$\boldsymbol{r} \to s^{1/\alpha}\boldsymbol{r}, \quad \boldsymbol{p} \to s^{1/2}\boldsymbol{p}, \quad t \to s^{1/2-1/\alpha}t \quad \text{for} \quad E \to sE\,. \tag{24}$$

Therefore, one only has to solve the classical dynamics once at a fixed energy, e.g. $E = U$; the results for all other energies are then simply given by the scale transformations (24) with $s = E/U$. This highly simplifies the POT analysis [28, 56].

With this, we are able to apply the POT to more realistic potentials, accounting for a finite diffuseness of the potential along the radial variable. Note that the definition (23) can also be generalized to include deformations (see, e.g., [56]).

3.4.1 *PERIODIC ORBITS IN THE RADIAL POWER-LAW POTENTIALS*

The definition (23) can be used in arbitrary dimensions, as long as r is the corresponding radial variable. In practice, we are interested only in the 2D and 3D cases. The spherical 3D and the circular 2D potential models have common sets of periodic orbits. They are labeled by integers $M(n_r, n_\varphi)$, where n_r and n_φ are mutually commensurable integers representing the number of oscillations in radial direction and the number of rotations around the origin, respectively, and M is again the repetition number. For the harmonic oscillator ($\alpha = 2$), all the classical orbits are periodic with (degenerate) ellipse shapes. By slightly varying α away from 2, the diameter and circular orbits remain as the shortest periodic POs. With increasing α, the circular orbit and its repetitions cause successive bifurcations, generating various new periodic orbits (n_r, n_φ) $(n_r > 2n_\varphi)$ (see Appendix A2 for details). Fig. 26 shows some of the shortest POs. The only difference between the periodic orbits in the 3D and 2D systems is their degeneracies. The shortest PO is the diameter

which has the degeneracy $\mathcal{K} = 1$ in the 2D system and $\mathcal{K} = 2$ in the 3D case at $\alpha > 2$. Other polygon-like orbits have, respectively, $\mathcal{K} = 1$ and $\mathcal{K} = 3$ at $\alpha > \alpha_{bif}$ where α_{bif} is the bifurcation value (A14). The circular orbit, having maximum angular momentum, is isolated ($\mathcal{K} = 0$) for the 2D system and has $\mathcal{K} = 2$ in the 3D case (except at the bifurcation points).

3.4.2 *TRACE FORMULA FOR 2D CIRCULAR POTENTIAL*

In the 2D circular potential, it is useful to take the angular momentum ℓ as one of the integration variables in the phase-space trace formula (3). The integration limits $\ell = \pm\ell_c$, given in (A9), correspond to the circular orbits moving anticlockwise (+) and clockwise (−).

For the contributions of the one-parametric families of the diameters and polygon-like POs, the integration over the cyclic angle variable φ conjugate to ℓ is easily carried out, and the remaining integration over ℓ is done within the simplest ISPM with finite limits $-\ell_c \leq \ell \leq \ell_c$. Thus, one obtains the ISPM trace formula in terms of error functions, as explained in sect. 3.1. Extending the integration limits to $\pm\infty$, one will arrive at the asymptotic Berry-Tabor trace formula [16], like in the cavity model. It is also worth noting that the limits $\alpha \to \infty$ and $\alpha \to 2$ of the derived ISPM trace formula successfully reproduce their asymptotic limits obtained previously for the circular billiard (disk) and the 2D isotropic harmonic oscillator, respectively.

The contribution of the isolated ($\mathcal{K} = 0$) circular orbits are derived by adopting the ISPM for two integrations over suitable (radial phase-space) variables. It yields a product of two error functions as shown in (9). Extension of the finite integration limits in both error functions to infinity (i.e., to $\pm\infty$ after their transformation to the corresponding Fresnel integrals of positive or negative real arguments) leads to the (SSPM) Gutzwiller amplitudes for the considered isolated POs [13].

The total semiclassical level density (5) is thus given by

$$g_{scl}(E) = g_{TF}(E) + \delta g^{(1)}_{scl}(E) + \delta g^{(0)}_{scl}(E) \tag{25}$$

with $\widetilde{g}\,(E) \approx g_{TF}(E)$ of the Thomas-Fermi model and

$$\delta g^{(\mathcal{K})}_{scl}(E) = \mathrm{Re} \sum_{po} \mathcal{A}^{(\mathcal{K})}_{po}(E) \exp\left[\frac{i}{\hbar} S_{po}(E) - \frac{i\pi}{2}\sigma^{(\mathcal{K})}_{po} - i\phi^{(\mathcal{K})}_{d}\right]. \tag{26}$$

The analytic expressions for the amplitudes $\mathcal{A}^{(\mathcal{K})}_{po}$ and phases $\sigma^{(\mathcal{K})}_{po}$ and $\phi^{(\mathcal{K})}_{d}$ are given in Appendix A3. Using the scale invariance (24), one may factorize the action integral $S_{po}(E)$ as

$$S_{po}(E) = \oint_{po(E)} \boldsymbol{p} \cdot d\boldsymbol{r} = \left(\frac{E}{U}\right)^{\frac{1}{2}+\frac{1}{\alpha}} \oint_{po(E=U)} \boldsymbol{p} \cdot d\boldsymbol{r} \equiv \hbar\varepsilon\tau_{po}. \tag{27}$$

In the last equation, we define dimensionless scaled energy ε and scaled period τ_{po} by

$$\varepsilon = \left(\frac{E}{U}\right)^{\frac{1}{2}+\frac{1}{\alpha}}, \qquad \tau_{po} = \frac{1}{\hbar}\oint_{po(E=U)} \boldsymbol{p}\cdot d\boldsymbol{r}. \tag{28}$$

To realize the advantage of the scaling invariance, it is helpful to use the scaled energy (period) in place of the corresponding original variables. For the harmonic oscillator one has $\alpha = 2$, and the scaled energy and period are proportional to the unscaled quantities. For the cavity potential ($\alpha \to \infty$), they are proportional to the momentum p and length L_{po}, respectively. The energy-scaled level density is written as

$$\delta g^{(\mathcal{K})}_{scl}(\varepsilon) = \frac{dE}{d\varepsilon}\delta g^{(\mathcal{K})}(E) = \mathrm{Re}\sum_{po}\mathcal{A}^{(\mathcal{K})}_{po}(\varepsilon)\exp\left[i\varepsilon\tau_{po} - \frac{i\pi}{2}\sigma^{(\mathcal{K})}_{po} - i\phi^{(\mathcal{K})}_{d}\right]. \tag{29}$$

This simple form of the phase function enables us to make use of the Fourier transformation technique again. The Fourier transform of the semiclassical energy-scaled level density with respect to the scaled period τ is given, like in Eq. (14), by

$$F(\tau) = \int \mathrm{d}\varepsilon\; g(\varepsilon)e^{i\varepsilon\tau} \sim F_0(\tau) + \sum_{po}\widetilde{\mathcal{A}}_{po}\delta(\tau-\tau_{po})\;, \tag{30}$$

which exhibits peaks at periodic orbits $\tau = \tau_{po}$. $F_0(\tau)$ represents the Fourier transform of the smooth TF level density and has a peak at $\tau = 0$ related to the direct (zero-action) trajectory, as discussed in Sect. 3.1. Thus, from the Fourier transform of the energy-scaled quantum-mechanical level density,

$$F(\tau) = \int\left[\sum_{n}\delta(\varepsilon-\varepsilon_n)\right]e^{i\varepsilon\tau}d\varepsilon = \sum_{n}e^{i\varepsilon_n\tau}, \qquad \varepsilon_n = \left(\frac{E_n}{U}\right)^{\frac{1}{2}+\frac{1}{\alpha}}, \tag{31}$$

one can directly extract information about the classical PO contributions.

3.4.3 *AMPLITUDE ENHANCEMENT AND COMPARISON WITH QUANTUM RESULTS*

Fig. 27 shows the typical enhancement phenomena owing to bifurcations of POs, e.g. for the case of the birth of the triangle-like PO $(3,1)$ from the simplest (primitive) circular orbit $(1,1)$. The scaled amplitudes $|\mathcal{A}_{sc,\,po}|$ are presented as functions of the power parameter α. In Fig. 27, the enhancement of the diameter amplitudes $|A_{sc,\,(2,1)}|$ and those $|A_{sc,\,(1,1)}|$ for the primitive circular orbit $(1,1)$ in the HO limit $\alpha \to 2$ are clearly shown. The second sharp peak in the circular PO amplitude $\mathcal{A}_{sc,\,(1,1)}$ near the bifurcation point $\alpha = 7$ is related to the bifurcation of the PO $(3,1)$ from the parent orbit $(1,1)$. Note that a rather wide maximum appears in the ISPM amplitude $|A_{sc\,(3,1)}|$ of the triangular-like orbit to the right of the bifurcation $\alpha = 7$ in Fig. 27, even larger than

for 3D orbits in the spheroidal cavity (see Sect. 3.3). [The third maximum in $|\mathcal{A}_{sc,\,(1,1)}|$ for a birth of the simplest quadrangle-like PO (4,1) at the bifurcation $\alpha = 14$ of the same parent-circular orbit is also seen, because the convergence of the ISPM triangle (3,1) amplitude $|\mathcal{A}_{sc,\,(3,1)}|$ to its SSPM asymptotics is realized within such a very wide region up to about $\alpha = 20$.] The ghost part of the $|A_{sc,\,(3,1)}|$ curve for α to the left of the bifurcation point $\alpha = 7$ is suppressed by rapid oscillations of the phase of a complex amplitude $A_{sc,\,(3,1)}$ with a frequency going to zero in the HO limit. It is similar like for all 3D PO ghosts in the spheroidal cavity in Sect. 3.3 (see also [20]), and for such one-parametric family POs in the integrable version of the 2D Hénon Heiles potential (see Fig. 4 in [21] for the arguments of the complex amplitude).

Divergences of $|A_{sc,\,(1,1)}|$ and discontinuities of $|A_{sc,\,(3,1)}|$ of the SSPM amplitudes are seen in Fig. 27, too. The continuous results of the improved SPM through the bifurcations (or symmetry-breaking points) are also seen with the characteristic enhancement.

Fig. 28 shows the Fourier transform of the energy-scaled quantum-mechanical level density (30). For a smaller $\alpha = 2.1$, the diameter (2,1) orbit makes the dominant contribution to the gross-shell structure as the shortest POs (see the peak at $\tau \sim 5.0$). With increasing α, the amplitude of the circular orbit becomes again larger and shows a prominent enhancement around the bifurcation point ($\tau \sim 6.2$ at $\alpha_{bif} = 7.0$). Near the bifurcation, the contribution of the newborn triangular-orbit family (3,1), having a higher degeneracy $\mathcal{K} = 1$, becomes also important and dominating for larger $\alpha > \alpha_{bif}$. [The newborn (3,1) peak again cannot be distinguished from the parent circular (1,1) orbit near the bifurcation point α_{bif}, like the diameter and circular orbits at α close to the HO limit.]

Fig. 29 shows a nice agreement of the fine-resolved semiclassical and the quantum level densities $\delta g_\gamma(\varepsilon)$ as functions of the scaled energy ε at the critical bifurcation points $\alpha = 7$ and 4.25 for the births of the triangle-like $(3,1)$ and the star-like $(5,2)$ orbits. For the semiclassical trace formula, see (16), we used

$$\delta g_{\gamma,\,scl}(\varepsilon) = \sum_{\mathcal{K}=0}^{1} \delta g^{(\mathcal{K})}_{\gamma,\,scl}(\varepsilon) = \sum_{\mathcal{K}=0}^{1} \sum_{po} \delta g^{(\mathcal{K})}_{po}(\varepsilon)\, \exp\left(-\tau^2_{po}\gamma^2/4\right), \tag{32}$$

where $\delta g^{(\mathcal{K})}_{po}(\varepsilon)$ is given by (29). For the quantum calculations we used the standard Strutinsky averaging (over the scaled energy ε), finding a good plateau around the Gaussian averaging width $\widetilde{\gamma} = 2 - 3$ with curvature-correction degree $\mathcal{M} = 6$. According to Eq. (12), for the corresponding shell correction energy δE_{scl} one obtains

$$\delta E_{scl}/U = \sum_i \varepsilon_i \delta n_i \simeq \frac{4\alpha}{\alpha+2}\, \varepsilon^{(3\alpha-2)/[2(\alpha+2)]} \sum_{\mathcal{K}=0}^{1} \sum_{po} \frac{1}{\tau^2_{po}}\, \delta g^{(\mathcal{K})}_{po}(\varepsilon_F)\,. \tag{33}$$

Here, δn_i are the variations of the occupation numbers defined by the Strutinsky smoothing procedure (see, e.g., [12]). Fig. 30 shows the scaled energy shell corrections δE_{scl} (33) as functions of the particle number $N^{1/2}$ by using the standard relationship $N = N(\varepsilon_F)$, see (13),

$$N = 2\int_0^{\varepsilon_F} g_{scl}(\varepsilon)\mathrm{d}\varepsilon \ . \tag{34}$$

A good plateau for the quantum calculations of the scaled energy shell corrections, see the first equation in (33), is realized near the same averaging parameters $\widetilde{\gamma}$ and $\mathcal{M}$ mentioned above. In the semiclassical calculations for the relation $N(\varepsilon_F)$, we integrated in (34) the semiclassical level density

$$g_{\gamma,\,scl}(\varepsilon) = g_{TF}(\varepsilon) + \sum_{\mathcal{K}=0}^{1} \delta g^{(\mathcal{K})}_{\gamma,\,scl}(\varepsilon) \ , \tag{35}$$

where $g_{TF}(\varepsilon)$ is the scaled average part obtained within the TF approximation [4],

$$g_{TF}(\varepsilon) = \frac{\alpha}{\alpha+2}\,\varepsilon \ , \tag{36}$$

and $\delta g^{(\mathcal{K})}_{\gamma,\,scl}(\varepsilon)$ of the ISPM was determined as discussed above. For the relation $N = N(\varepsilon_F)$ we used specifically an averaging in small $\gamma = 0.1$ because there is almost no sensitivity of this integral characteristics within the interval of smaller γ ($\gamma = 0.02 - 0.1$). The PO sums converge for the averaging width $\gamma = 0.2$ of a fine resolution of the shell structure and energy shell corrections with taking into account the major simplest POs [about 4 repetition numbers for the circular and diameter ($M = 4$) and a few first simplest other $\mathcal{K} = 1$ POs like (3,1), (5,2), (7,3) and (8,3)] which are important at $\alpha = 7$. As seen from Figs. 29 and 30, we obtain a nice agreement between the semiclassical (ISPM, solid) and quantum (QM, dotted) results. Notice that the dominating contributions in these semiclassical results at the bifurcation point $\alpha = 7$ are coming from the bifurcating circular $(1,1)$ and newborn (3,1) orbits, while the bifurcating circular $2(1,1)$ and star-like $(5,2)$ orbits are important for $\alpha = 4.25$, as expected from enhancement of their amplitudes seen in Fig. 27. The POs (3,1) and (5,2) yield more contributions near the bifurcation values of α and even more on their right in a wide region of α as mentioned above. The orbits (1,1), (3,1) [or (2(1,1),(2,5)] give essential ISPM contributions of about the same order of magnitude and phase in the upper (or lower) panels of Figs. 29 and 30, respectively. Notice that the newborn POs (5,2), (7,3) and (8,3) give comparable contributions in this Figure, in nice agreement with the quantum Fourier spectra Fig. 28.

The nice beating seen in these figures is explained by the interference of these orbits with the simple diameters of the same order in magnitude but with different phases. The latter ISPM contributions are close to the SSPM asymptotic ones near the bifurcation points $\alpha = 7$ and 4.25, because

they are far enough away from their only symmetry-breaking point at the harmonic oscillator value $\alpha = 2$.

4 SUMMARY AND CONCLUSIONS

In the first part (Sect. 2) of this article we have given a short review of Strutinsky's shell-correction method (SCM). It was conceived as a practicable tool for numerical realizations of the theory of finite interacting fermion systems, developed by Migdal and collaborators, in particular at times when computers were not sufficiently fast to perform fully selfconsistent microscopic calculations. The SCM, primarily applied to atomic nuclei, combines the average binding (or deformation) energies from the classical liquid drop model with a microscopic shell-correction energy δE that is extracted from the quantum-mechanical energy spectra of realistic (deformed) nuclear shell models. It was and still is used world wide for very successful computations, in close agreement with experimental data, of nuclear masses and deformation energies, in particular fission barriers.

In a second and larger part (Sect. 3), we have presented a semiclassical theory of quantum oscillations, based upon Gutzwiller's trace formula which connects the level density of a quantum system to a sum over periodic orbits (POs) of the corresponding classical system. This periodic orbit theory (POT) was extended by Strutinsky and collaborators and applied to express the shell-correction energy δE of a finite fermion system in terms of POs. The semiclassical trace formulae for δE exhibit a rapid convergence of the PO sum, due to an inverse dependence of the individual orbit contributions on the squares of their periods (lengths) (see Sect. 3.1). This allows one often to express significant features of the shell structure in terms of a few short periodic orbits. In many cases, the shortest POs are sufficient to describe the gross-shell features in δE.

Bifurcations of periodic orbits can have a significant influence on a fermionic quantum system and leave signatures in its energy spectrum (visualized, e.g., by its Fourier transform) and hence its shell structure. We have (in Sect. 3.1) presented a general method to incorporate bifurcations in the POT, employing an improved stationary-phase method (ISPM) based on the theory of Fedoryuk and Maslov, and hereby overcoming the divergence of the semiclassical amplitudes of the Gutzwiller theory at bifurcations. The improved semiclassical amplitudes typically exhibit a clear enhancement near a bifurcation and on that side of it where new orbits emerge (see, e.g., Figs. 14, 15 and 27), which is of the order $\hbar^{-1/2}$ in the semiclassical parameter $\hbar$. This, in turn, leads to enhanced shell structure effects.

In Sect. 3.2, we have presented a semiclassical calculation of a typical actinide fission barrier us-

ing the POT, employing a fission cavity model that uses a realistic description of the three principal axially-symmetric deformations (elongation, neck formation and left/right asymmetry) occurring in the (adiabatic) fission process (see Fig. 4). The characteristic (static) double-humped barrier (Fig. 3) and, in particular, the sensitivity of the outer barrier to left/right-asymmetric deformations can be qualitatively well described by the POT (Fig. 8). The loci of minimal quantum shell-correction energies δE, both in particle number vs. deformation space (Fig. 5) and in two-dimensional deformation space (Fig. 10), are correctly followed by the constant-action loci of the shortest POs. Hereby we observe a clear signature of period-one bifurcations of the shortest equatorial orbits which here were treated semiclassically using normal forms and uniform approximations.

In Sect. 3.3, we have summarized the results of the spheroidal cavity model which had early been used in POT calculations for semiclassical investigations of nuclear deformations (see Fig. 2). This integrable system allows for analytical calculation of the PO properties. We show that the bifurcations of longer orbits, semiclassically treated with the ISPM, have an important influence on the shell structure of this system. More particularly, the bifurcated period-two and period-three orbits start to dominate the shell structure at medium (axis ratio $\eta \sim 1.5$) and larger deformations. In the superdeformed region $\eta \sim 1.6 - 2$, they dominate the minima of the shell-correction energy δE, the more the larger the particle number (especially at $\eta \sim 2$), due to their enhanced semiclassical amplitudes, and the shortest (period-one) orbits have only a little influence (Figs. 20 and 21). The quantum-mechanical Fourier spectra of the spheroidal cavity exhibit a nice quantum-to-classical correspondence, in that enhanced Fourier signals follow exactly the lengths of the semiclassically enhanced classical POs (Fig. 25). This correspondence appears also in the correct description of the loci of large deformations in particle number vs. deformation space by the constant-action lines of the bifurcated period-two and -three orbits (see Fig. 24). An important reason for their strong enhancement at large deformations, besides the general argument given above (and explained in Sect. 3.1), is also the fact that the new bifurcated orbits have a larger classical degeneracy ($\mathcal{K} = 2$) than their parent orbits and the period-one orbits ($\mathcal{K} = 1$) (except near the bifurcations). This is not so in the fission cavity model (Sect. 3.2), where all POs (and all POs bifurcating from them) have the degeneracy $\mathcal{K} = 1$. (Another reason for differences between the two cavity models is, of course, the different deformation space used by them, which leads, amongst others, to a shift of critical deformations to larger values in the spheroidal cavity.)

In Sect. 3.4 we have, finally, presented a class of radial power-law potentials $V(r) \propto r^{\alpha}$, which turn out as good approximations to the popular Woods-Saxon potential in the spatial region where the particles are bound. The advantage of the power-law potential is that, in spite of its diffuse

surface, the classical dynamics scale with simple powers of the energy, which makes it particularly easy for POT calculations. The quantum Fourier spectra yield directly the lengths of the leading classical POs (Fig. 28). We have developed semiclassical trace formulae for this potential and study various limits of the power α (harmonic oscillator potential for $\alpha = 2$, cavity potential for $\alpha \to \infty$). Bifurcations are, again, treated in the ISPM leading to semiclassical enhancement of the orbit amplitudes. The trace formulae are shown numerically to give good agreement with the quantum-mechanical level density oscillations (Fig. 29) and shell-correction energies (Fig. 30).

In conclusion, we may state that the semiclassical theory (POT) is well capable of explaining the main features of quantum shell structure in terms of a few classical periodic orbits. Bifurcations of POs are not simply an obstacle of the semiclassical theory, but they leave clear signatures both in the quantum Fourier spectra and the locations of minima of the shell-correction energy δE plotted versus particle number and deformations.

In our future work we intend to further study finer shell structures due to longer orbits, applying both the ISPM and uniform approximations to treat their bifurcations. In particular, we want to understand the "quantization" into isolated minima that occurs along the valleys of both the ground-state and the secondary (isomer) minima and, in particular, we want to better understand the superdeformed shell structure. In the region of superdeformation in the spheroidal cavity, we see clearly from Fig. 24 that this is due to the bifurcated period-two and -three orbits. It will be interesting to study the analogue situation in the fission cavity model by investigating the higher-period bifurcations occurring there. One complication in that model is that we have to vary three deformation parameters (c, h, α), instead of only one (η) for the spheroid, in order to fully cover the fission barrier landscape. This will naturally lead to a much larger variety of possible bifurcations. Another object of our studies will be to understand semiclassically the transition regions between the downgoing ground-state valleys and the initially upgoing secondary-minimum valleys (see Figs. 5 and 23). They are well described separately by the shortest meridional and equatorial orbits, respectively, but in the transition regions ($1.2 \lesssim c \lesssim 1.35$ and $1.2 \lesssim \eta \lesssim 1.5$, respectively) we expect further bifurcations and corresponding new orbits to play a role. As a more technical aspect, we also want to perform detailed comparisons between the results obtained with the ISPM and the uniform approximations for specific bifurcations.

On a longer time scale, we intend also to include pairing and spin-orbit interactions into the POT calculations, in order to come closer to a realistic description of nuclei, and to extend the POT towards dynamics (e.g., studying inertial moments, friction coefficients, etc.). We keep in mind and emphasize, however, that the POT is not intended as a substitute for a fully quantum-mechanical

theory, but rather a tool for a better understanding of its results in terms of classical pictures.

Acknowledgement

We are very grateful to our late teachers, Profs. A. B. Migdal and V. M. Strutinsky, for so many creative ideas and collaborations. We also thank Profs. K. Matsuyanagi and E. E. Saperstein for fruitful collaborations and many useful discussions.

Appendix A:
2D RADIAL POWER-LAW POTENTIAL

A1. Classical Dynamics in Generic 2D Circular Hamiltonians

For an isotropic 2D potential $V(r)$, the Hamiltonian H in the canonical phase-space variables $\{r, \varphi, p_r, p_\varphi\}$ writes

$$H = \frac{1}{2m}\left(p_r^2 + \frac{p_\varphi^2}{r^2}\right) + V(r) = E\ . \tag{A1}$$

Here, $p_\varphi = \ell$ is the angular momentum, φ is the cyclic variable,

$$\varphi = \omega_\varphi t + \varphi'\ , \tag{A2}$$

$\varphi' = \varphi(t = t' = 0)$ is the initial condition,

$$p_r(r) \equiv \sqrt{p^2(r) - \frac{\ell^2}{r^2}} = \sqrt{2m\left[E - V(r)\right] - \frac{\ell^2}{r^2}} = m\dot{r}, \qquad p(r) = \sqrt{2m\left[E - V(r)\right]}\ . \tag{A3}$$

In particular, we shall consider the power-law potential (23) from [28].

Integrating the first equation in (A3) one has also the radial trajectory $r(t)$,

$$m\int_{r'}^{r} \frac{\mathrm{d}\rho}{\sqrt{2m\left[E - V(\rho)\right] - \ell^2/\rho^2}} = t\ , \tag{A4}$$

where $r' = r(t = t' = 0)$ as the initial condition for the radial coordinate r. For the radial action I_r in polar action-angle variables over one period ($t = T$) with $\varphi' = \varphi''$ ($r' = r''$) one has

$$\begin{aligned} I_r &= \frac{1}{2\pi}\oint p_r\,\mathrm{d}r = \frac{1}{\pi}\int_{r_{min}}^{r_{max}} \mathrm{d}r\,\sqrt{2m\left[E - V(r)\right] - \frac{\ell^2}{r^2}} = I_r(E, \ell), \\ I_\varphi &= \frac{1}{2\pi}\oint p_\varphi\,\mathrm{d}\varphi = \ell\ , \end{aligned} \tag{A5}$$

where r_{min} and r_{max} are the turning points for a given energy E, which are solutions of the equation:

$$\mathcal{F}(r, \ell) \equiv 2m\left[E - V(r)\right] - \frac{\ell^2}{r^2} = 0\ . \tag{A6}$$

For frequencies one has

$$\omega_r = \frac{\partial H}{\partial I_r} = \frac{1}{\partial I_r/\partial E} = \left(\frac{m}{\pi}\int_{r_{min}}^{r_{max}} \frac{\mathrm{d}r}{\sqrt{2m\left[E - V(r)\right] - \ell^2/r^2}}\right)^{-1}\ , \tag{A7}$$

where $I_r = I_r(E, \ell)$ is the surface energy (A5). Thus, the periodic-orbit equation writes

$$f(\ell) \equiv \frac{\omega_\varphi}{\omega_r} \equiv -\frac{\partial I_r(E, \ell)}{\partial \ell} \equiv \frac{\ell}{\pi}\int_{r_{min}}^{r_{max}} \frac{\mathrm{d}r}{r^2\sqrt{2m\left[E - V(r)\right] - \ell^2/r^2}} = \frac{n_\varphi}{n_r}\ , \tag{A8}$$

n_φ and n_r are co-primitive integers. The energy surface $I_r = I_r(E, \ell)$ is simplified to function of one variable ℓ. The solutions to the PO equation (A8) for $\ell = \ell^*(n_r, n_\varphi)$ define the $\mathcal{K} = 1$ families of orbits $M(n_r, n_\varphi)$, see [15].

A2. Circular Orbit in Power-Law Potential

In the radial power-law potential (23), the isolated circular orbits cause successive bifurcations with increasing α. At the energy E, the radius of a circular orbit is given by

$$r_c = R\left(\frac{2E}{(2+\alpha)U}\right)^{1/\alpha}, \qquad \ell_c = p(r_c)r_c, \qquad \mathcal{F}_c'' = -\frac{4m\,E\alpha}{r_c^2} < 0, \tag{A9}$$

$\mathcal{F}_c$ is defined by (A6). The radial frequency $\Omega_c = \omega_r(r_c)$ is given by

$$\Omega_c = \sqrt{\frac{\alpha(2+\alpha)U}{mR^2}}\,\left[\frac{2E}{(2+\alpha)U}\right] > 0. \tag{A10}$$

From (A7) at $\ell = \ell_c$ by using (A9) for r_c and ℓ_c one finds [28]

$$\omega_c = \omega_\varphi(\ell = \ell_c) = \sqrt{\frac{\alpha U}{mR^2}}\,\left(\frac{2E}{(2+\alpha)U}\right)^{1/2-1/\alpha}. \tag{A11}$$

From (A10) and (A11), one has the equation,

$$\frac{\Omega_c}{\omega_c} = \frac{n_r}{n_\varphi}\,, \tag{A12}$$

given explicitly by [28]

$$\sqrt{2+\alpha} = \frac{n_r}{n_\varphi}\,. \tag{A13}$$

Thus, for the bifurcation diffuseness parameter α_{bif} where the one-parametric orbits (n_r, n_φ) are born one arrives at the explicit expression:

$$\alpha_{bif} = n_r^2/n_\varphi^2 - 2\,. \tag{A14}$$

A3. Trace formula for 2D Circular Power-Law Potential Model

From the ISPM procedure presented in sect. 3.1, we obtain contributions of the $\mathcal{K} = 1$ families and isolated circular orbits into the semiclassical level density. For a $\mathcal{K} = 1$ family, we choose the angular momentum ℓ and angle φ conjugate to ℓ for integration variables in the phase-space trace formula (3). The integration over a cyclic angle φ generates only the factor 2π. The remaining integration over ℓ is carried out within the simplest ISPM by expanding a phase function Φ in powers of $\ell - \ell^*$ up to quadratic terms. [The expansion of pre-exponent factor of integrand in powers of $\ell - \ell^*$ is cut at zero order in this approximation.]

Thus, we obtain the amplitude $\mathcal{A}_{po}^{(1)}$ of Eq. (26) as

$$\mathcal{A}_{po}^{(1)} = \frac{T_{po}}{\pi\hbar^{3/2}\sqrt{M n_r\,|K_{po}|}}\;\mathrm{erf}(\mathcal{Z}_{po}^-, \mathcal{Z}_{po}^+) \tag{A15}$$

with the period

$$T_{po} = \frac{2\pi n_r}{\omega_r} = \frac{2\pi n_\varphi}{\omega_\varphi} \,, \tag{A16}$$

K_{po} is the curvature of the energy surface,

$$K = \frac{\partial^2 I_r}{\partial I_\varphi^2} = \frac{\partial^2 I_r(E,\ell)}{\partial \ell^2} = -\frac{\partial f(\ell)}{\partial \ell}, \tag{A17}$$

$f(\ell)$ is the ratio of frequencies defined in the first three equations of (A8). The arguments of the generalized complex error function in (A15), see also (10), is given by

$$\mathcal{Z}_{po}^{\pm} = \sqrt{-i\pi M n_r \left|K_{po}\right|/\hbar}\, b_{po}\left(\ell_\pm - \ell_{po}\right) , \tag{A18}$$

where $b_{po} = 1$ for all $\mathcal{K} = 1$ polygon-like PO families, except for the diameters for which one has (see [21])

$$b_{M(2,1)} = 1 - \frac{1}{2}\,\exp\left[-\left(\frac{\alpha-2}{2\Delta_D}\right)^2\right], \qquad \Delta_D = \frac{1}{\sqrt{\pi M n_r K_D/\hbar}}, \tag{A19}$$

K_D is the diameter curvature. For simplicity, the finite integration interval of the angular momenta was split into two parts, $-\ell_c \le \ell \le 0$ and $0 \le \ell \le \ell_c$, where ℓ_c is the angular momentum of a circular orbit as mentioned above. There are the symmetric stationary points $\pm|\ell^*|$ related to the clockwise and anticlockwise motion of the particle along the PO in these two parts of the phase space. They give equivalent contributions to the amplitude owing to the independence of the Hamiltonian of time. Thus, we have reduced the integration region to $0 \le \ell \le \ell_c$ accounting for this time-reversibility symmetry simply by a factor 2 in (A15). Therefore, for the polygon-like ($n_r > 2$) POs, one has $\ell_{=}0$ and $\ell_+ = \ell_c$. In the HO limit $\alpha \to 2$, only the diameter (2,1) and the circle (1,1) (with repetitions) survive and form $\mathcal{K} = 2$ families in the HO potential. It is natural to assume that the whole phase-space in the HO limit can be split into the two equivalent parts, $0 < \ell < \ell_c/2$ for the diameter and $\ell_c/2 < \ell < \ell_c$ for the circular orbits, for the angular momenta and correspondingly for the conjugate angles. Thus, we arrive at the integration limits (A18) with (A19). The same prescription has been successfully applied to the integrable version of the Hénon-Heiles potential for contributions of orbits B and A in the same HO limit [21]. For the Maslov index of the considered $\mathcal{K} = 1$ family of POs, one obtains

$$\sigma_{po}^{(1)} = 2Mn_r, \tag{A20}$$

and for the constant phase independent of the orbits one has $\phi_d = -\pi/4$.

Extension of the limit $\ell_\pm \to \pm\infty$ exactly reproduces the asymptotic Berry-Tabor formula [16, 4]

$$\mathcal{A}_{po}^{(1)} = \frac{d_{po} T_{po}}{\pi\hbar^{3/2}\sqrt{M n_r \left|K_{po}\right|}} \,, \tag{A21}$$

where d_{po} takes into account the discrete degeneracy, $d_{po} = 1$ for diameters $M(2,1)$ ($n_r = 2n_\varphi$) and 2 for all other POs ($n_r > 2n_\varphi$) [4]. In the circular billiard limit ($\alpha \to \infty$), the action $S_{po}(E)$ is given by

$$S_{po}(E) = pL_{po}, \qquad p = \sqrt{2mE}\,, \tag{A22}$$

and the curvature K_{po} from (A17) is obtained explicitly by

$$K_{po} = \frac{1}{\pi p R \sin\phi}\,. \tag{A23}$$

Substituting these quantities, Eqs. (A22) and (A23), into (A21), from (26) and (A20) one obtains the Balian-Bloch trace formula for the circular billiard [4].

For the contribution of circular orbits, one should perform the two exact phase-space integrations over radial variables within ISPM. Finally, we arrive at the result:

$$\mathcal{A}^{(0)}_{c,M} = \frac{T_c}{2\pi\hbar\sqrt{F_{c,M}}}\,\mathrm{erf}(\mathcal{Z}^{(-)}_{pc}, \mathcal{Z}^{(+)}_{pc})\,\mathrm{erf}(\mathcal{Z}^{(-)}_{rc}, \mathcal{Z}^{(+)}_{rc}), \tag{A24}$$

where T_c is the period of a primitive circular orbit. $F_{c,M}$ is its stability factor [13] given by

$$F_{c,M} = 4\sin^2\left[\pi M\sqrt{\alpha+2}\right]. \tag{A25}$$

The arguments of the complex error functions in (A24) are given by

$$\begin{aligned}
\mathcal{Z}^{(\pm)}_{p\,c} &= \sqrt{-\frac{i}{\hbar}\,\pi\,M\,\sqrt{\alpha+2}\left|K_c\right|}\;(\ell_\pm - \ell_c)\,, \qquad \ell_+ = \ell_c, \qquad \ell_- = \ell_c/2\,, \\
\mathcal{Z}^{(\pm)}_{r\,c} &= \sqrt{\frac{i\,F_{c,M}}{4\pi\,M\,\hbar\,\sqrt{\alpha+2}\,\left|K_c\right|}}\;\Theta^{(\pm)}_r\,, \qquad \Theta^{(+)}_r = \pi, \qquad \Theta^{(-)}_r = 0\,,
\end{aligned} \tag{A26}$$

where K_c is the circular-orbit curvature,

$$K_c = -\frac{(\alpha+1)(\alpha-2)}{12\,(\sqrt{\alpha+2})^3\,\ell_c}\,. \tag{A27}$$

The time-reversibility of the Hamiltonian was similarly taken into account as explained above. For the Maslov index one has $\sigma^{(0)}_{po} = 4M$ and $\phi_d = 0$. (The detailed derivation will appear elsewhere.) In the asymptotic limit of the finite non-zero integration boundaries $\ell_- \to -\infty$ and $\Theta^+_r \to \infty$, i.e. far from any bifurcations α_{bif} (also from the harmonic oscillator symmetry breaking at $\alpha = 2$), the expression (A24) tends to the amplitude of the Gutzwiller trace formula for isolated orbits [13, 4].

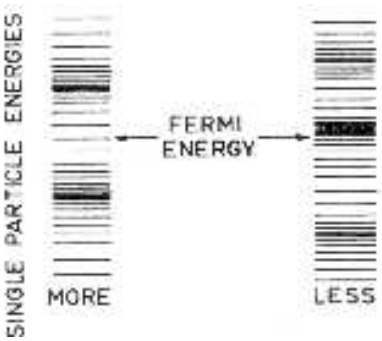


Figure 1: Schematic picture showing the relation of local level density at the Fermi energy to the binding of the system. Left side: Low level density – more bound; right side: high level density – less bound.

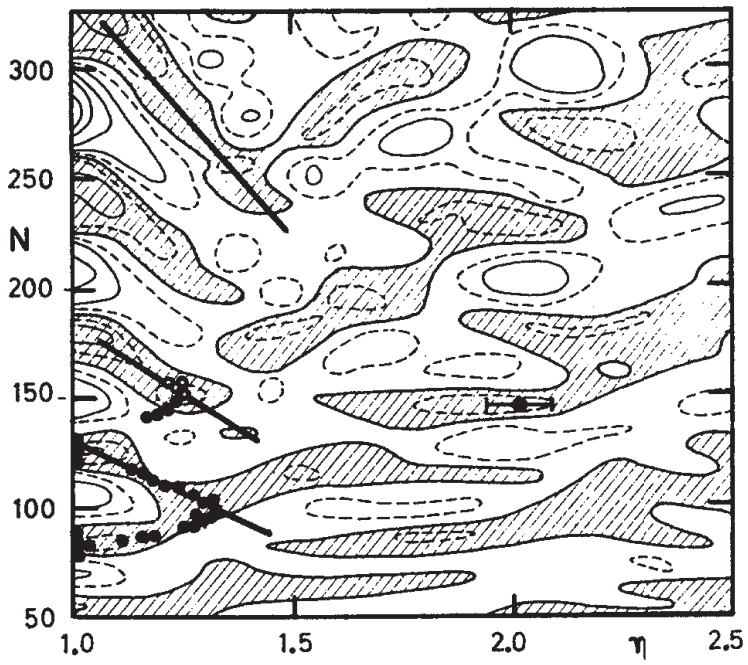


Figure 2: Neutron energy shell-correction $\delta E_n(N, \eta)$ for a realistic nuclear Woods-Saxon potential (with spin-orbit term), versus neutron number N and axis ratio η of the spheroidally deformed potential (equidistance: 2.5 MeV, areas with negative values are shaded). Dots indicate experimental deformations. The heavy bars are the semiclassical predictions for the loci of the ground-state minima using the leading classical periodic orbit families in a spheroidal cavity.

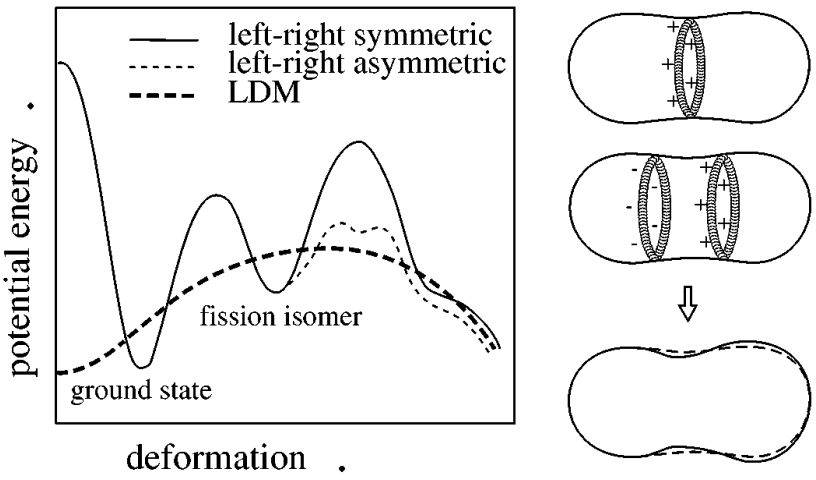


Figure 3: *Left:* Schematic double-humped fission barrier of a typical actinide nucleus. Note the lowering of the outer barrier due to left-right asymmetric shapes. *Right:* Maximum probability amplitudes (schematic) of the two leading s.p. states responsible for the asymmetry effect.

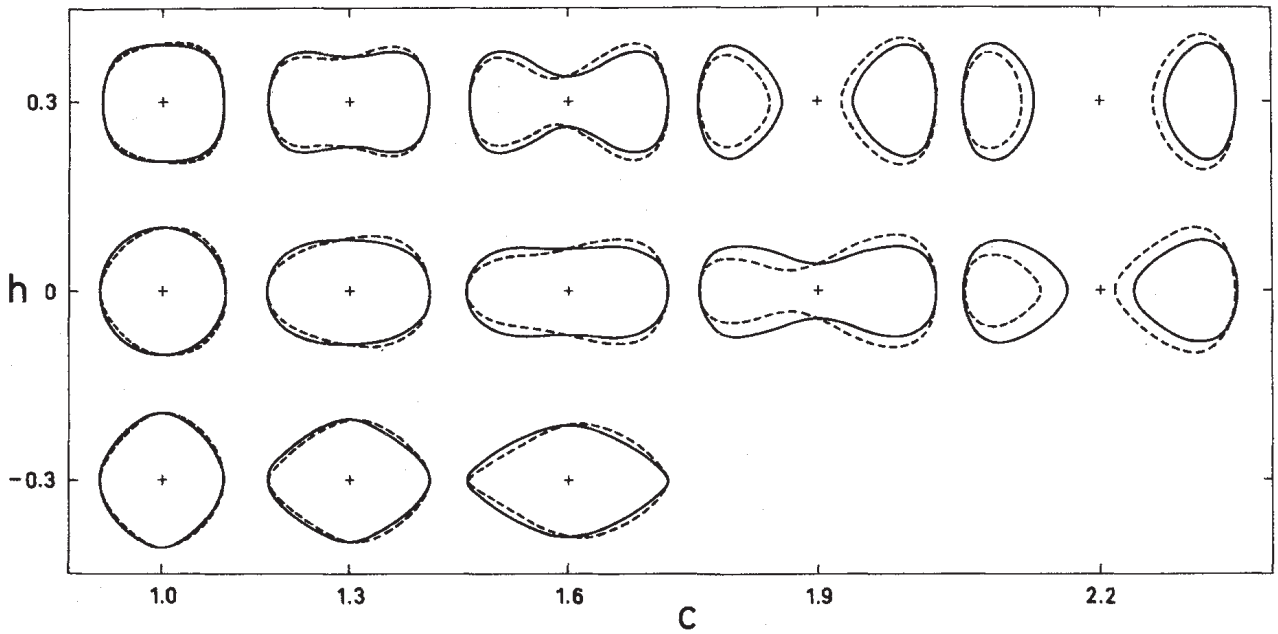


Figure 4: Axially symmetric nuclear shapes in the (c, h, α) parameterization of [12]. Dashed lines for $\alpha \neq 0$; the sequence with $h = \alpha = 0$ corresponds to the shapes obtained in the LDM [33].

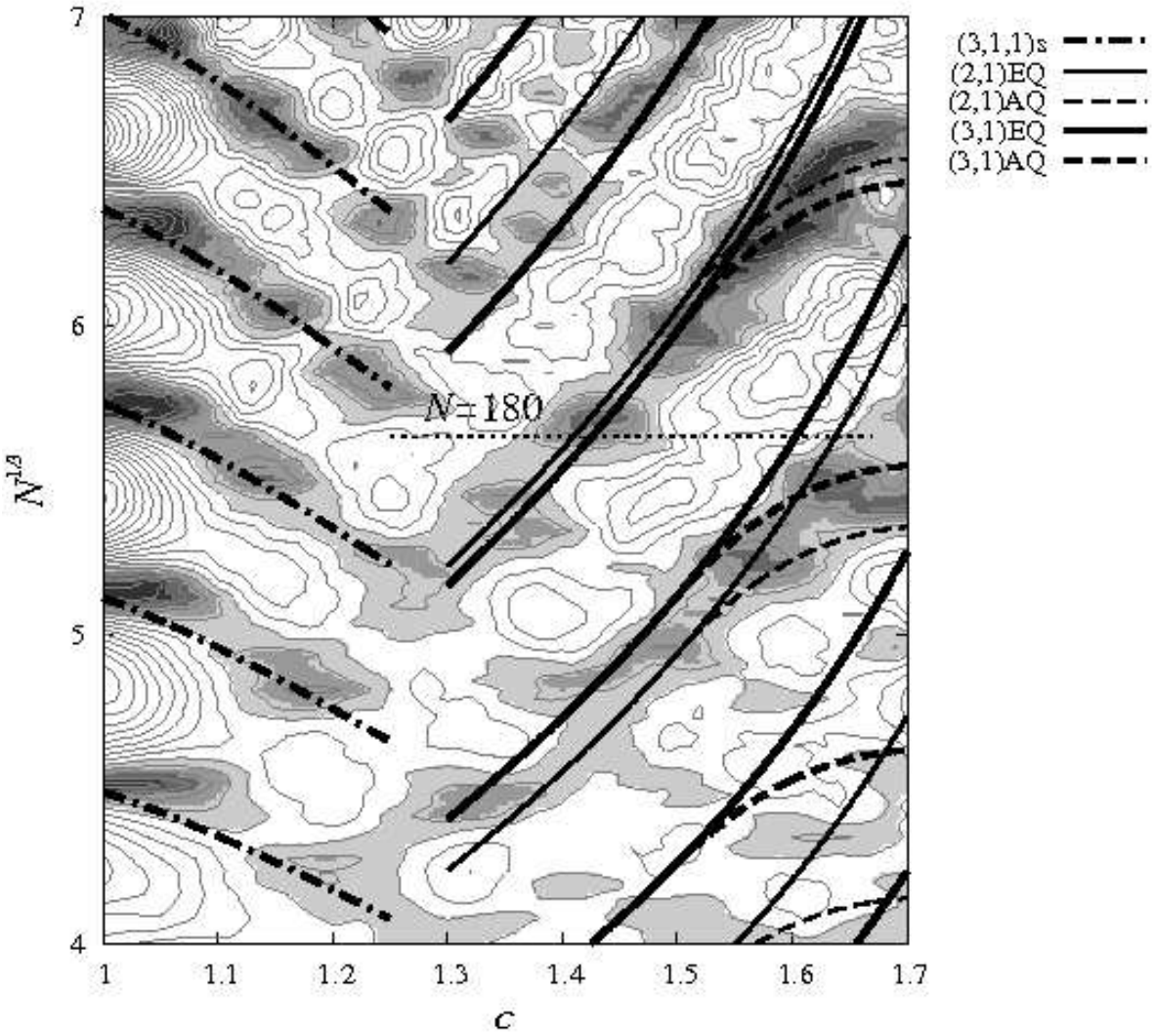


Figure 5: Plot of quantum-mechanical shell-correction energy δE versus cube-root of particle number, $N^{1/3}$, and elongation c (along $h = \alpha = 0$) in the cavity model. The contours lines are for constant values of δE (*white:* positive values, *gray to black:* negative values. The heavy lines indicate the loci of constant actions of the leading POs. *Dashed-dotted lines:* meridional triangular orbits (3,1,1)s; *narrow lines:* diameter orbits in equatorial planes (2,1)EQ (solid) and in parallel perpendicular planes (2,1)AQ (dashed); *broad lines:* triangular orbits in equatorial planes (3,1)EQ (solid) and in parallel perpendicular planes (3,1)AQ (dashed). The horizontal dotted line at $N \simeq 180$ corresponds to the situation with the isomer minimum at the correct deformation [12] $c \simeq 1.42$ of the real nucleus ^{240}Pu.

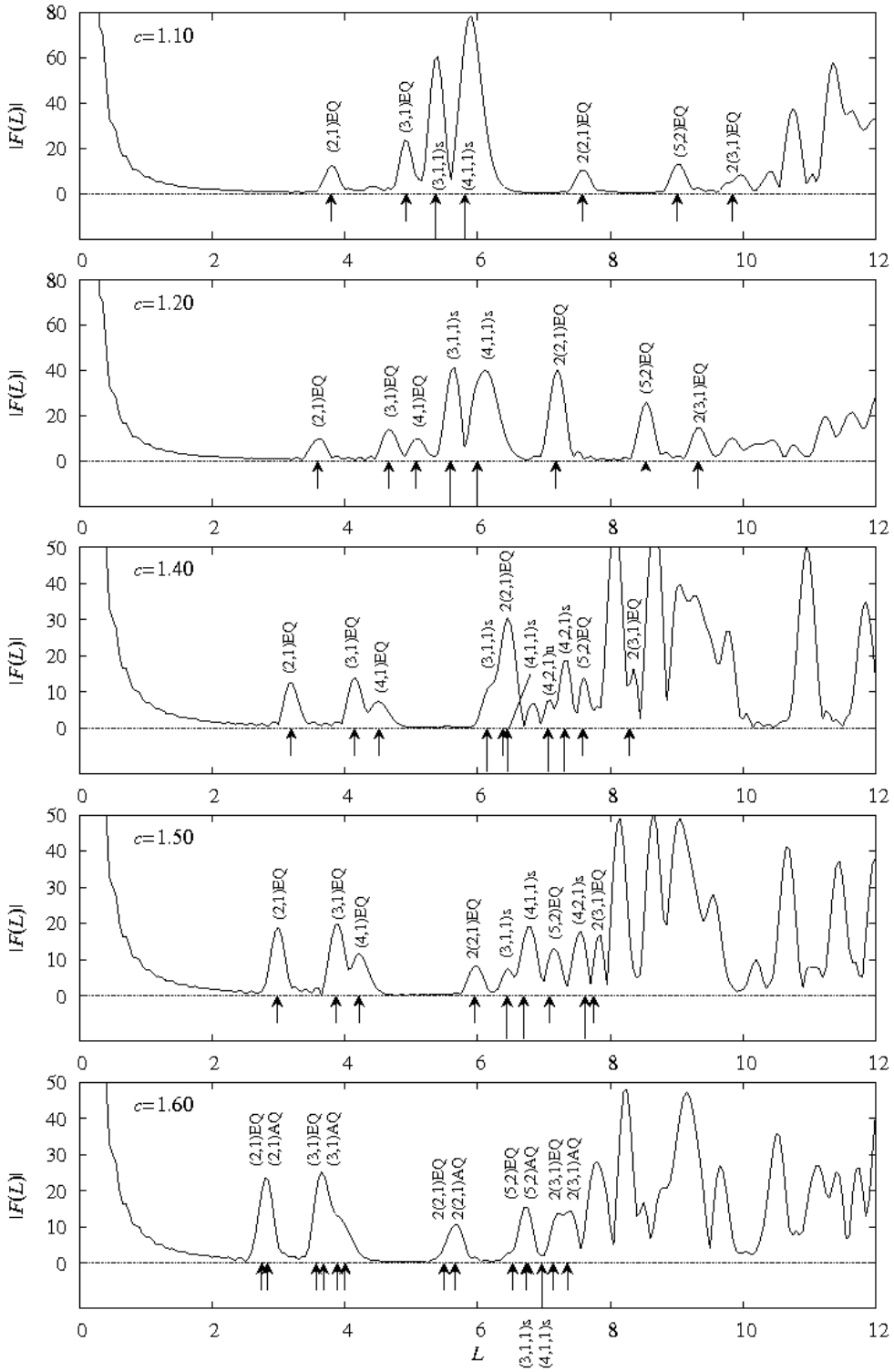


Figure 6: Fourier spectra of the fission cavity model with $h = \alpha = 0$ for five values of c: amplitude of Fourier transform of the quantum spectrum versus length L (in units of R_0) of the classical POs. *Short arrows:* POs lying in planes orthogonal to symmetry axis; *long arrows:* POs lying in meridional planes containing the symmetry axis (labels as in Fig. 5; see text for more details).

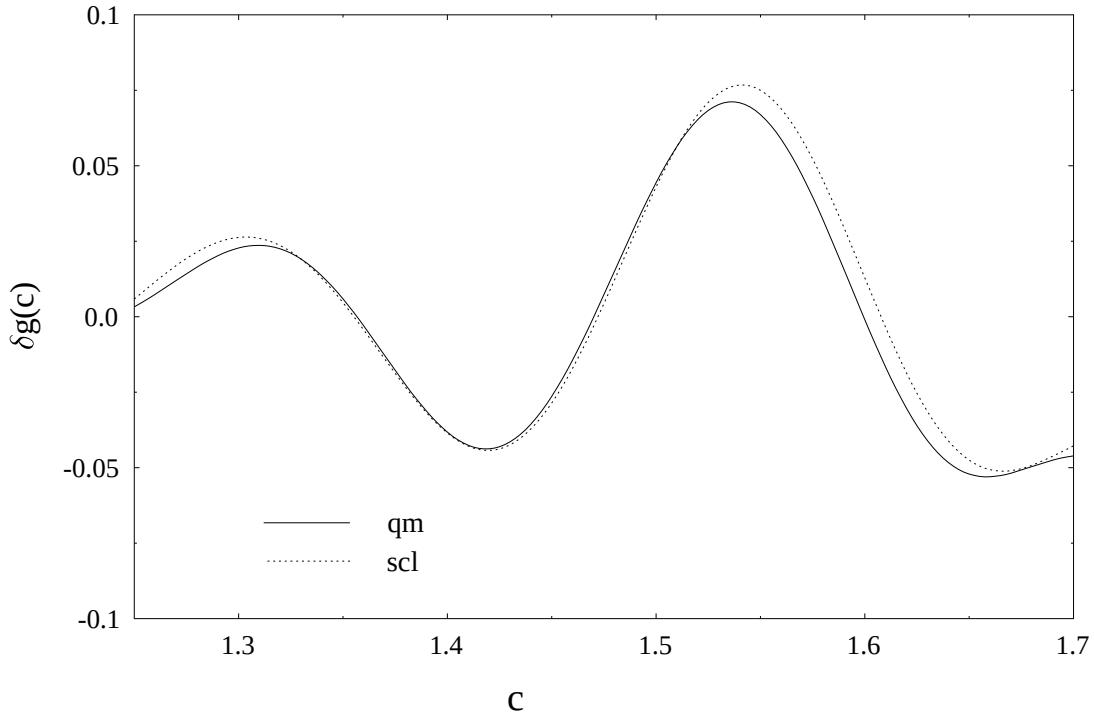


Figure 7: Quantum-mechanical (solid line) and semiclassical (dashed line) level density δg versus elongation c (along $h = \alpha = 0$) in the fission cavity model taken at the Fermi wave number $k_F = 12.1/R_0$. (Gaussian averaging over wave number k with width $\gamma = 0.6/R_0$.)

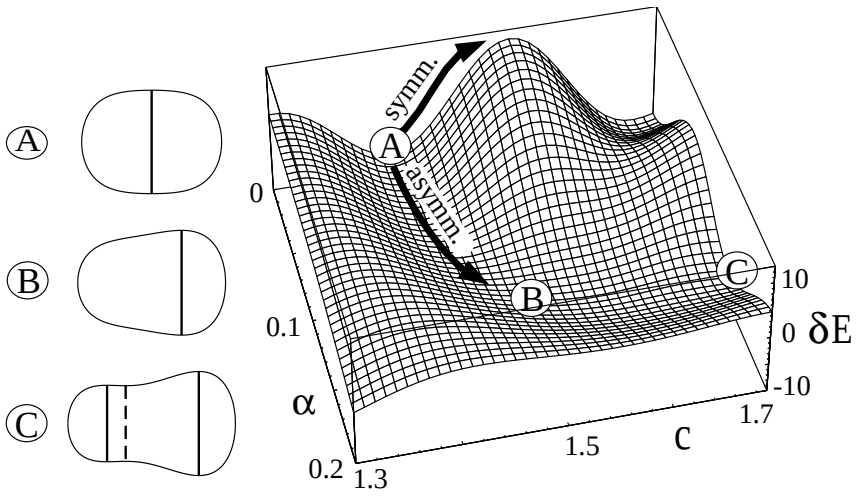


Figure 8: Perspective view of the semiclassical outer fission barrier versus elongation c and left-right asymmetry α for $h = 0$. To the left, the shapes corresponding to the points A, B and C in the deformation energy surface are displayed; the vertical solid (dashed) lines indicate the planes containing the stable (unstable) POs.

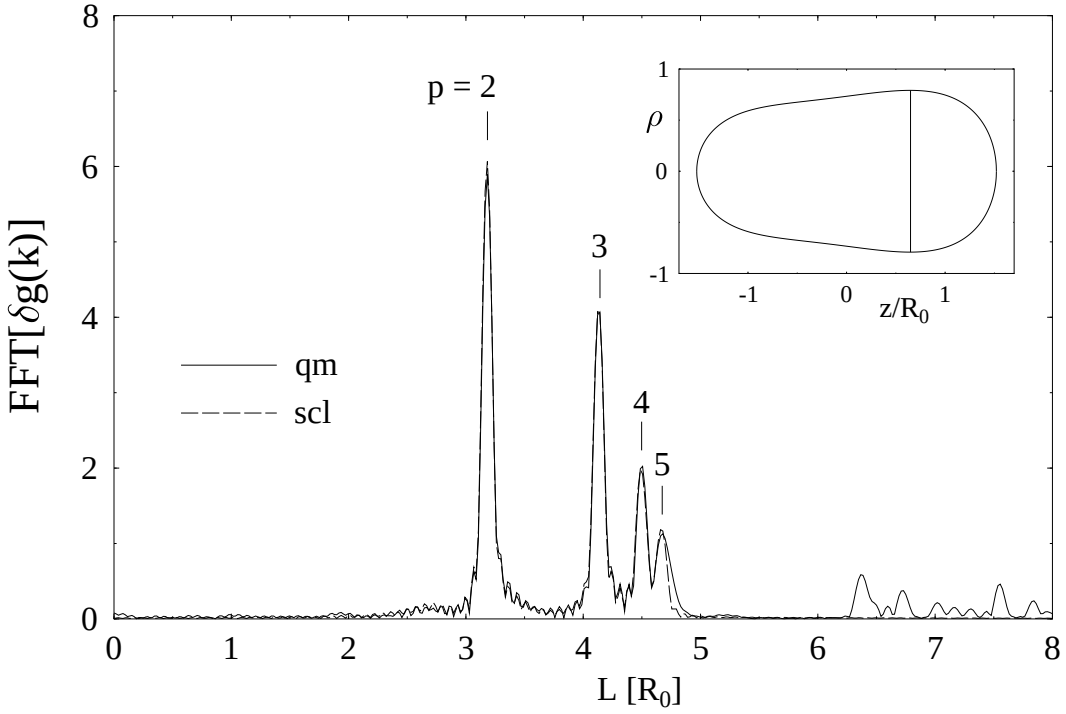


Figure 9: Squared amplitudes of the Fourier transforms of $\delta g(k)$ obtained (as in Fig. 7) quantum mechanically (solid line) and semiclassically (dashed line) for c=1.5, h=0, α=0.12. The insert shows the cavity shape and the location (vertical line) of the plane containing the shortest POs with reflection number p. The abscissa shows the length L of the POs in units of the spherical-cavity radius R_0; see the text for further details.

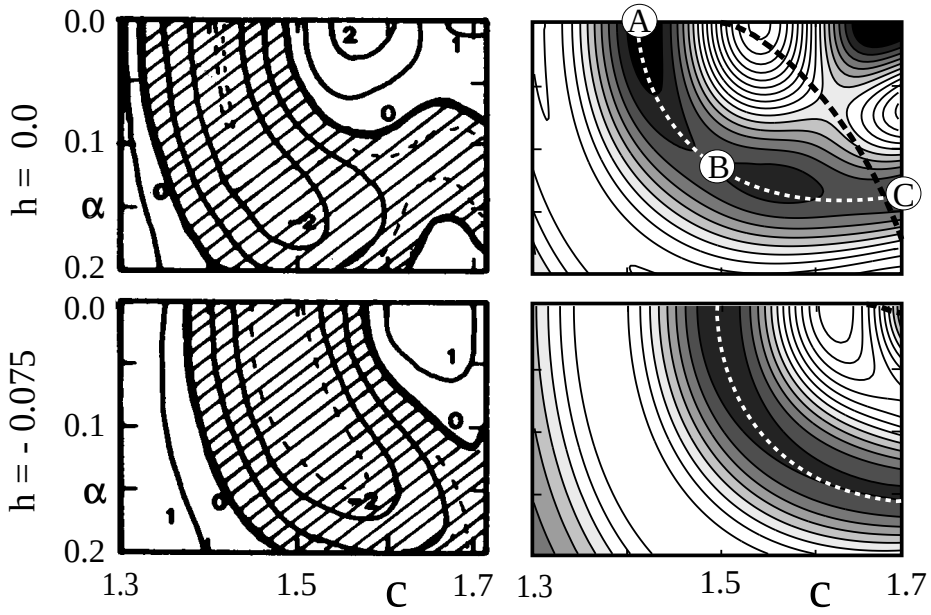


Figure 10: Contour plots of the shell-correction energy δE versus c and α. *Upper panels:* for $h = 0$, *lower panels:* for $h = -0.075$. *Left panels:* results of quantum-mechanical SCM calculations with realistic nuclear shell model potentials [12] (shown is the shell correction of the neutrons); *right panels:* semiclassical POT results with the fission cavity model described above.

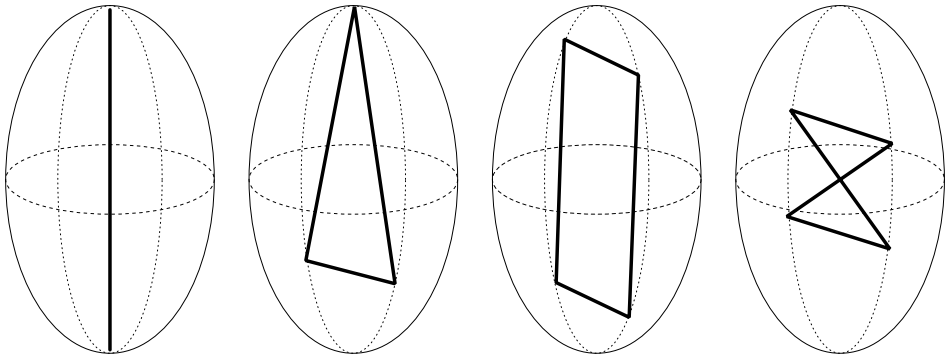


Figure 11: POs $M(n_u, n_v, n_\varphi)$ in the spheroidal cavity model: 2D orbits.

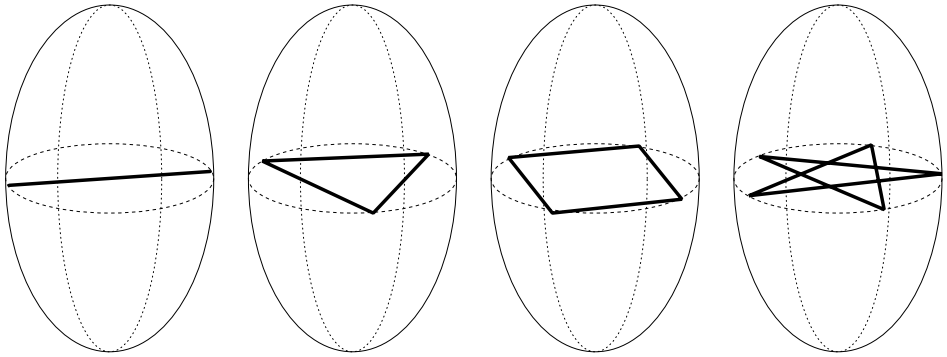


Figure 12: POs $M(n_u, n_v, n_\varphi)$ in the spheroidal cavity model: EQ orbits.

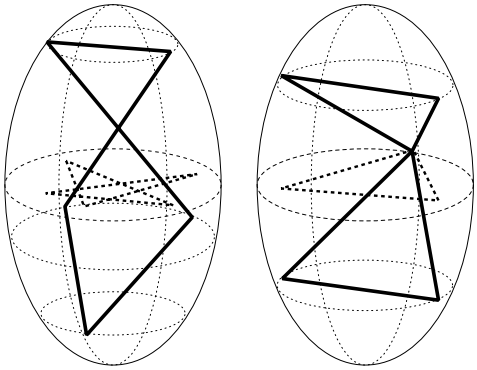


Figure 13: POs $M(n_u, n_v, n_\varphi)$ in the spheroidal cavity model: 3D orbits.

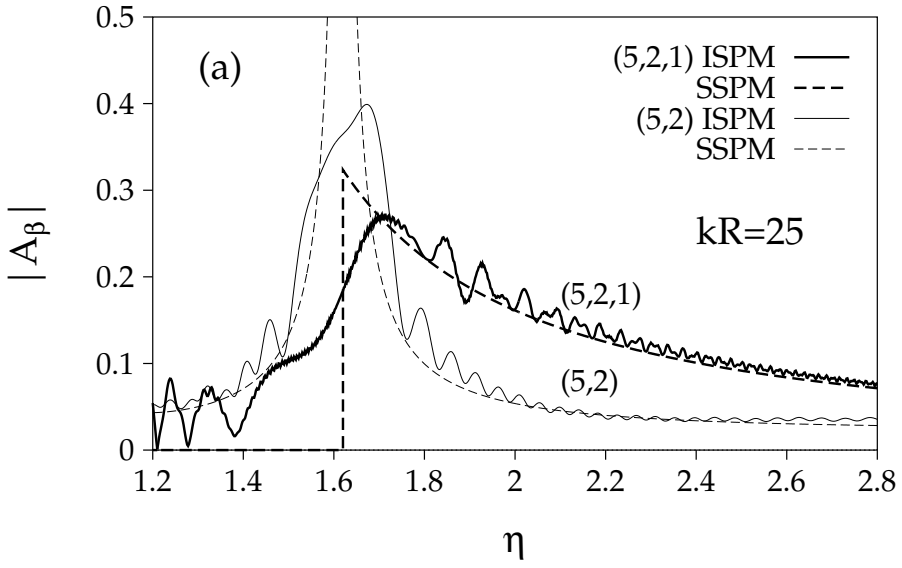


Figure 14: Amplitudes $\mathcal{A}_{5,2,1}$. Solid and dotted lines show the quantum and semiclassical ISPM results, respectively.

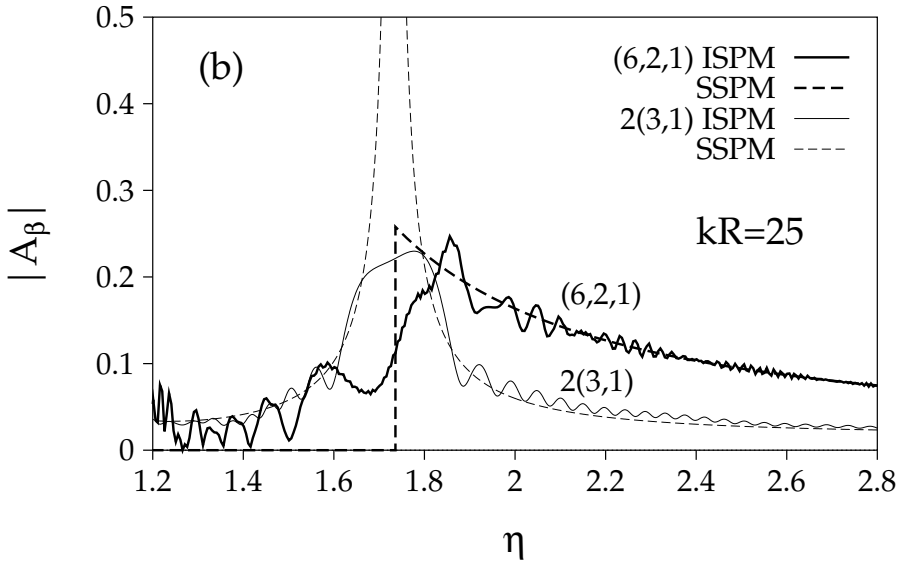


Figure 15: Amplitudes $\mathcal{A}_{6,2,1}$. Solid and dotted lines show the quantum and semiclassical ISPM results, respectively.

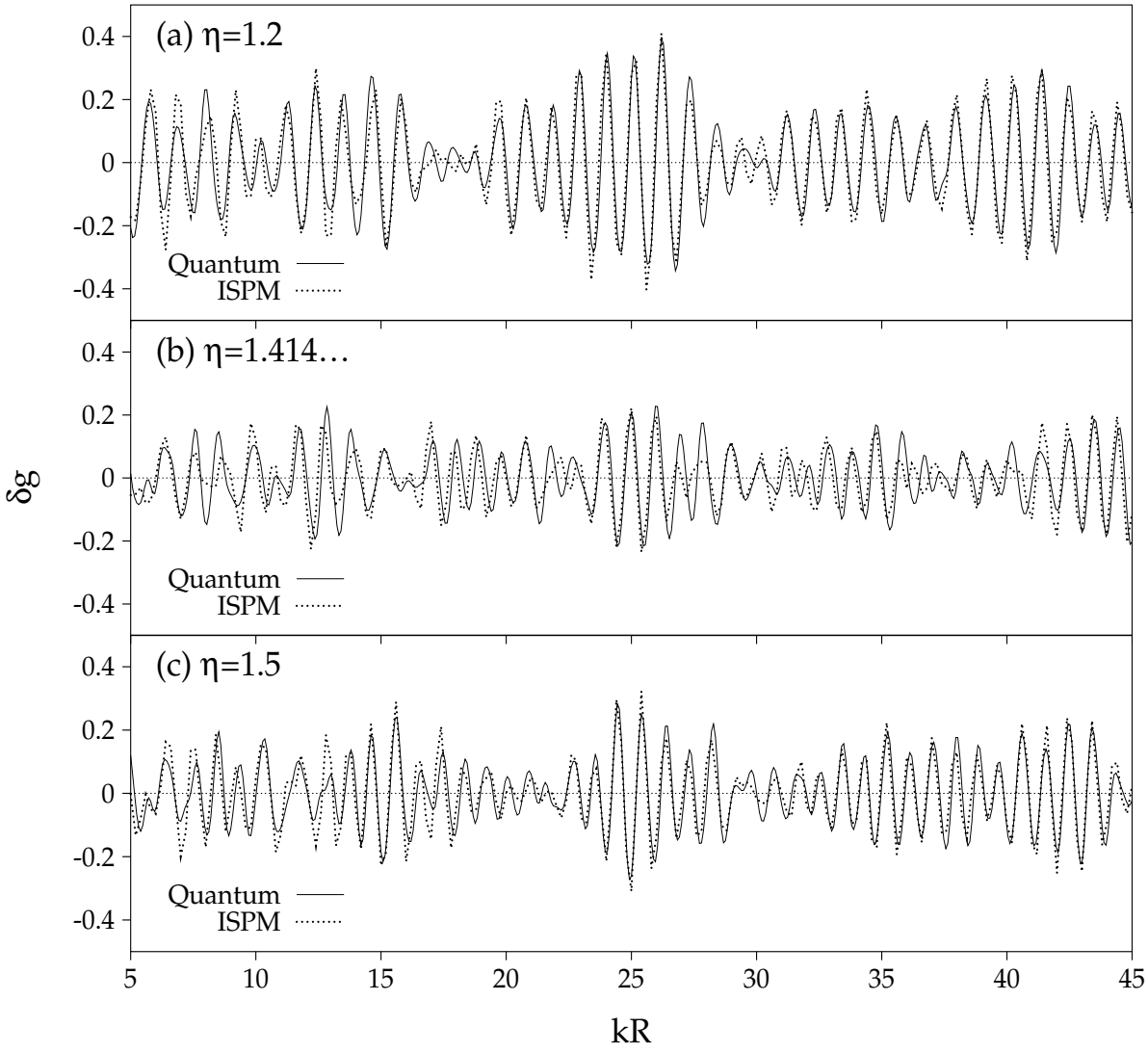


Figure 16: Oscillating part of level density $\delta g(k)$ in the spheroidal cavity (in units of $2mR^2/\hbar^2$, where R is the radius of the cavity at $\eta = 1$), plotted versus kR, for three specific deformations η. The Gaussian averaging parameter is $\gamma = 0.3/R$.

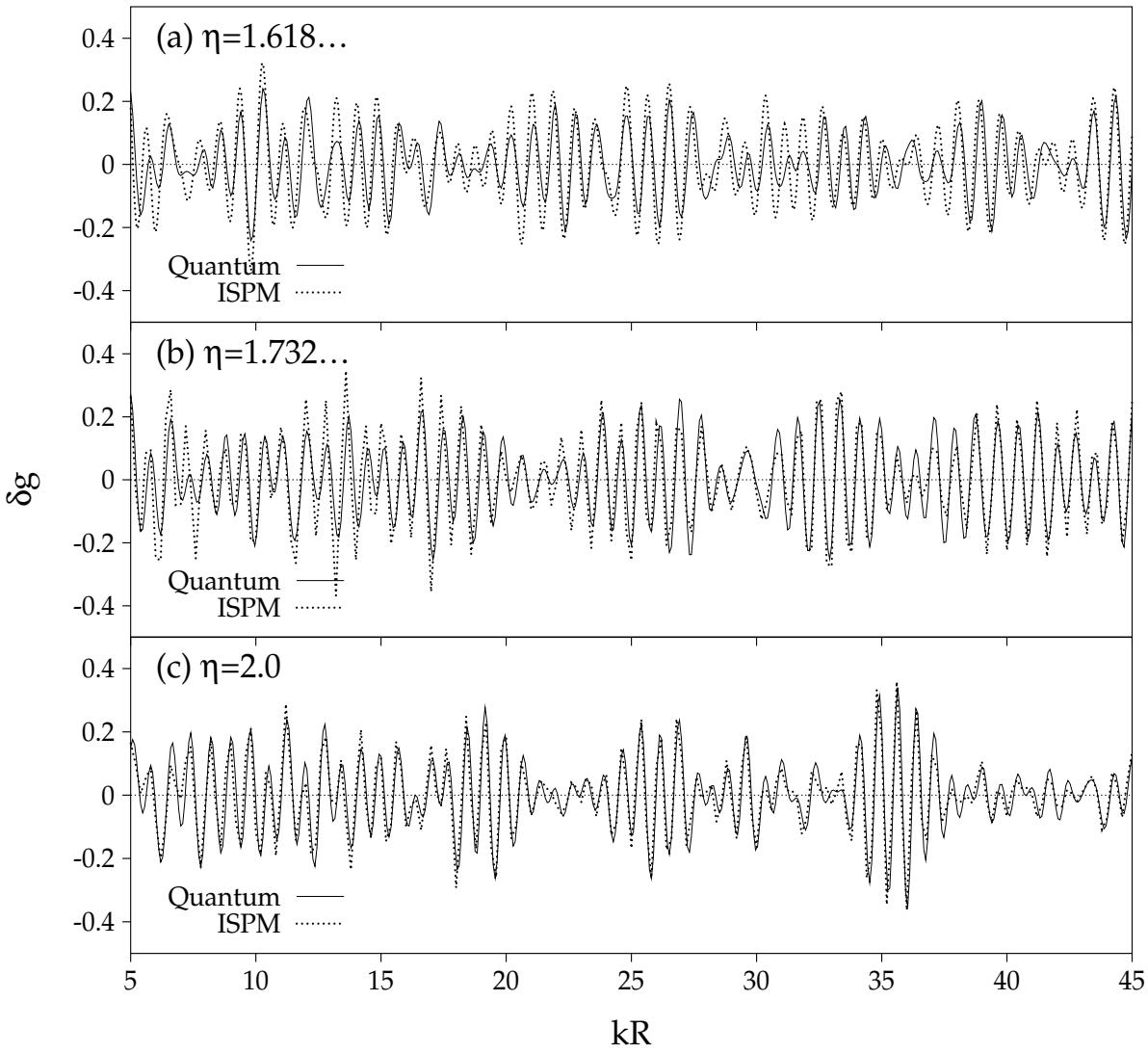


Figure 17: The same as in Fig. 16 but for three deformations in the superdeformed region.

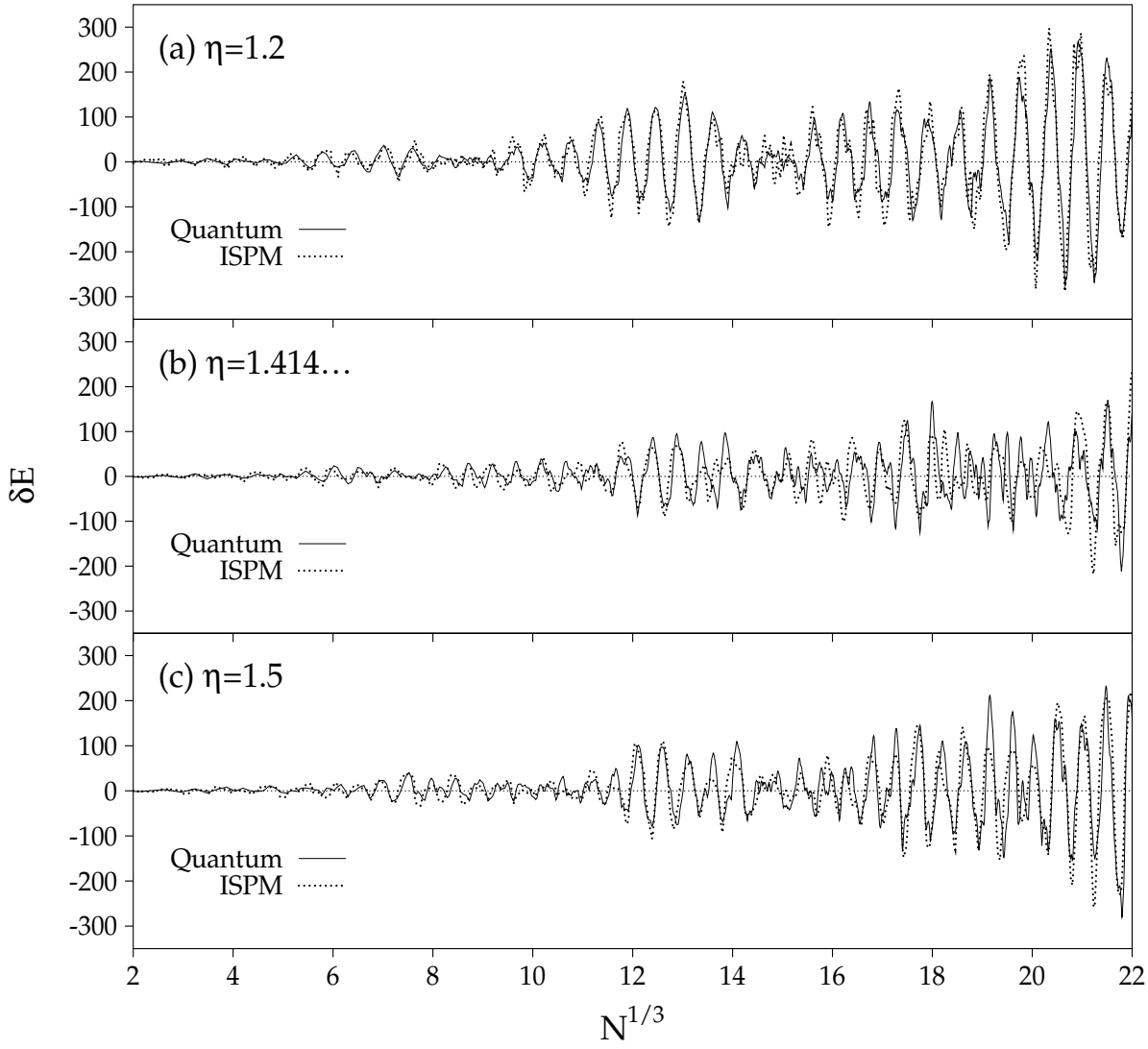


Figure 18: Shell-correction energy δE (in units of $\hbar^2/2mR^2$) vs. cube root of particle number $N^{1/3}$ for the same three deformations as in Fig. 16.

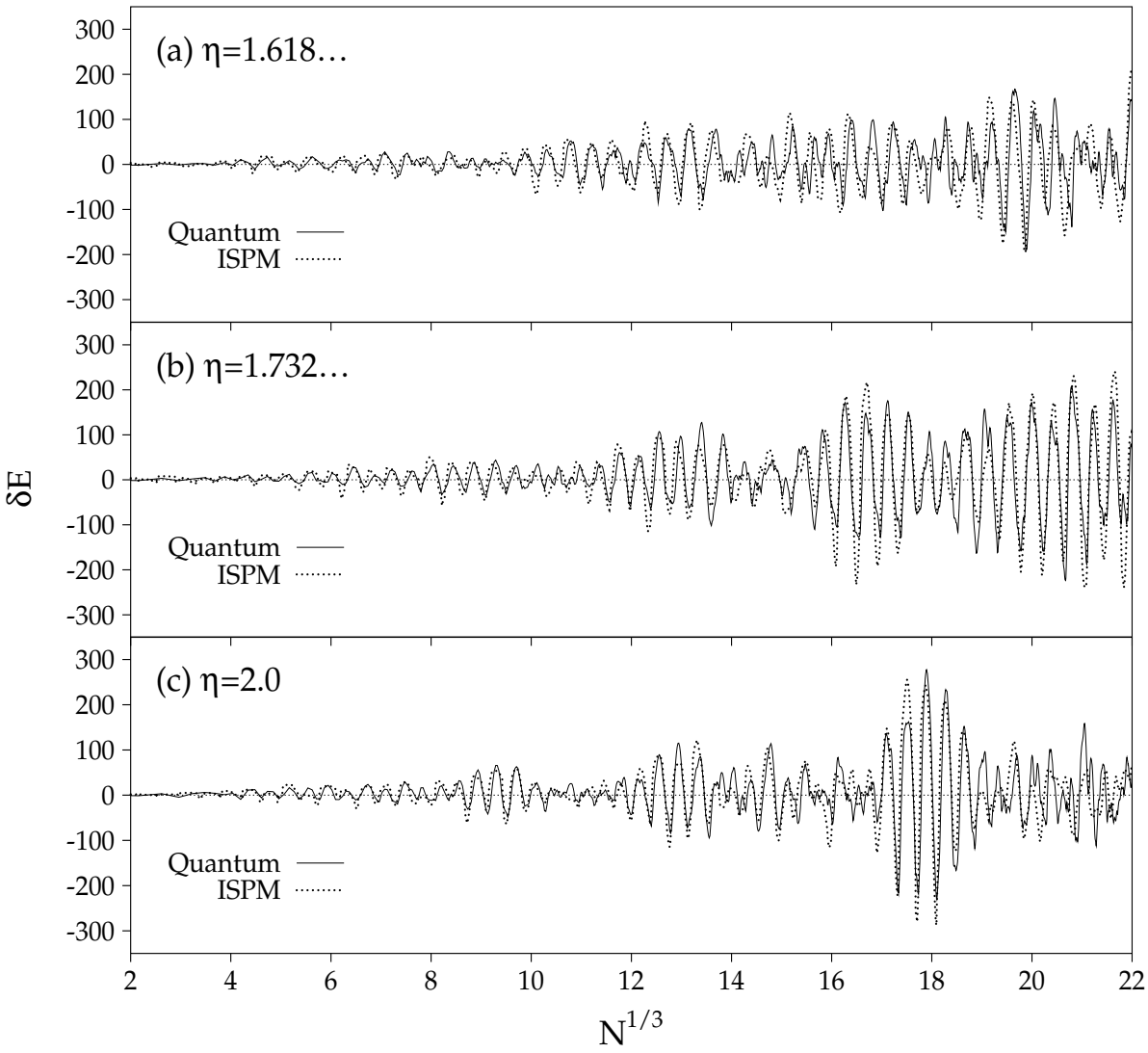


Figure 19: The same as in Fig. 18 but for the three deformations of Fig. 17.

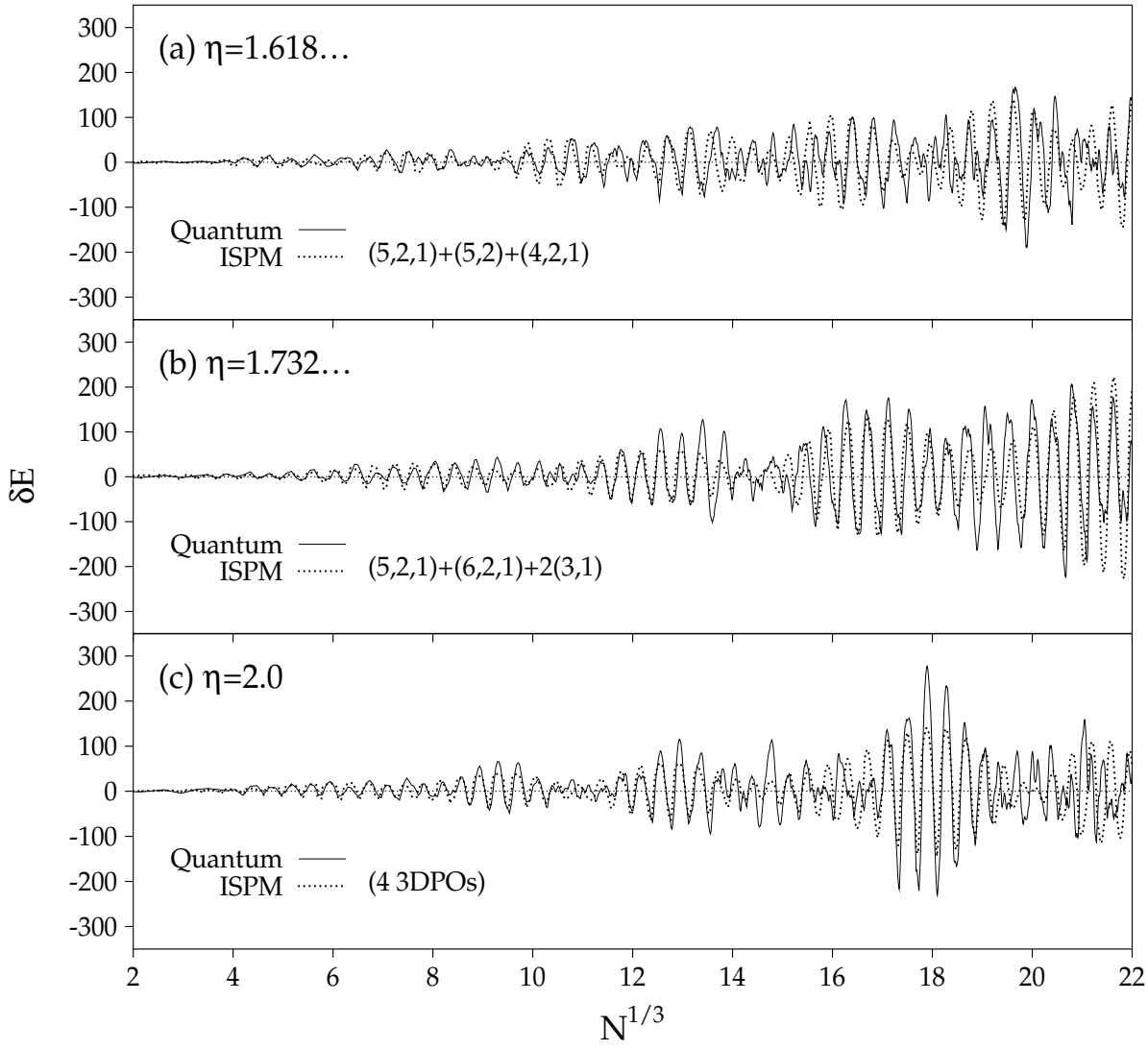


Figure 20: The same as in Fig. 19 in the superdeformation region, but the semiclassical results (ISPM) here include only the bifurcated period-two and -three orbits specified near the dotted lines "ISPM".

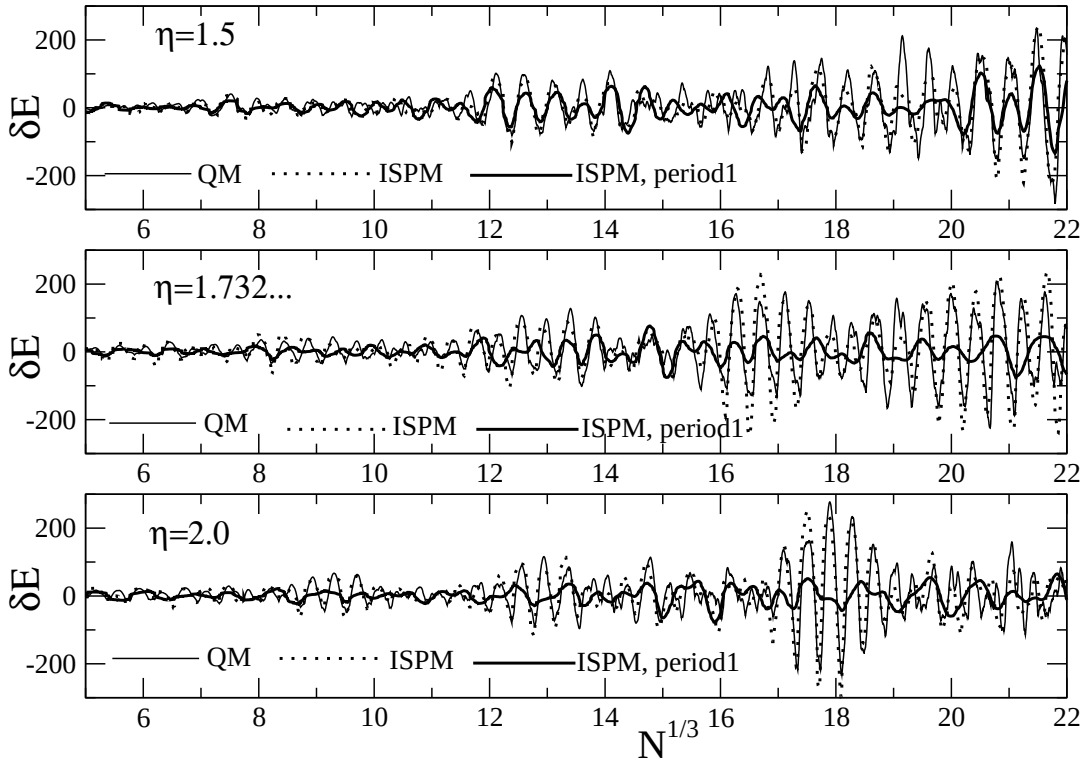


Figure 21: Shell-correction energy δE (in units of $\hbar^2/2mR^2$) vs. cube root of particle number $N^{1/3}$ for the characteristic deformations $\eta = 1.5$, 1.732... and 2.0. Solid lines are the quantum results, dots represent the ISPM results including the bifurcating period-two orbits. The thick solid lines show the ISPM results obtained using only the shortest EQ and meridional orbits (see text for discussion).

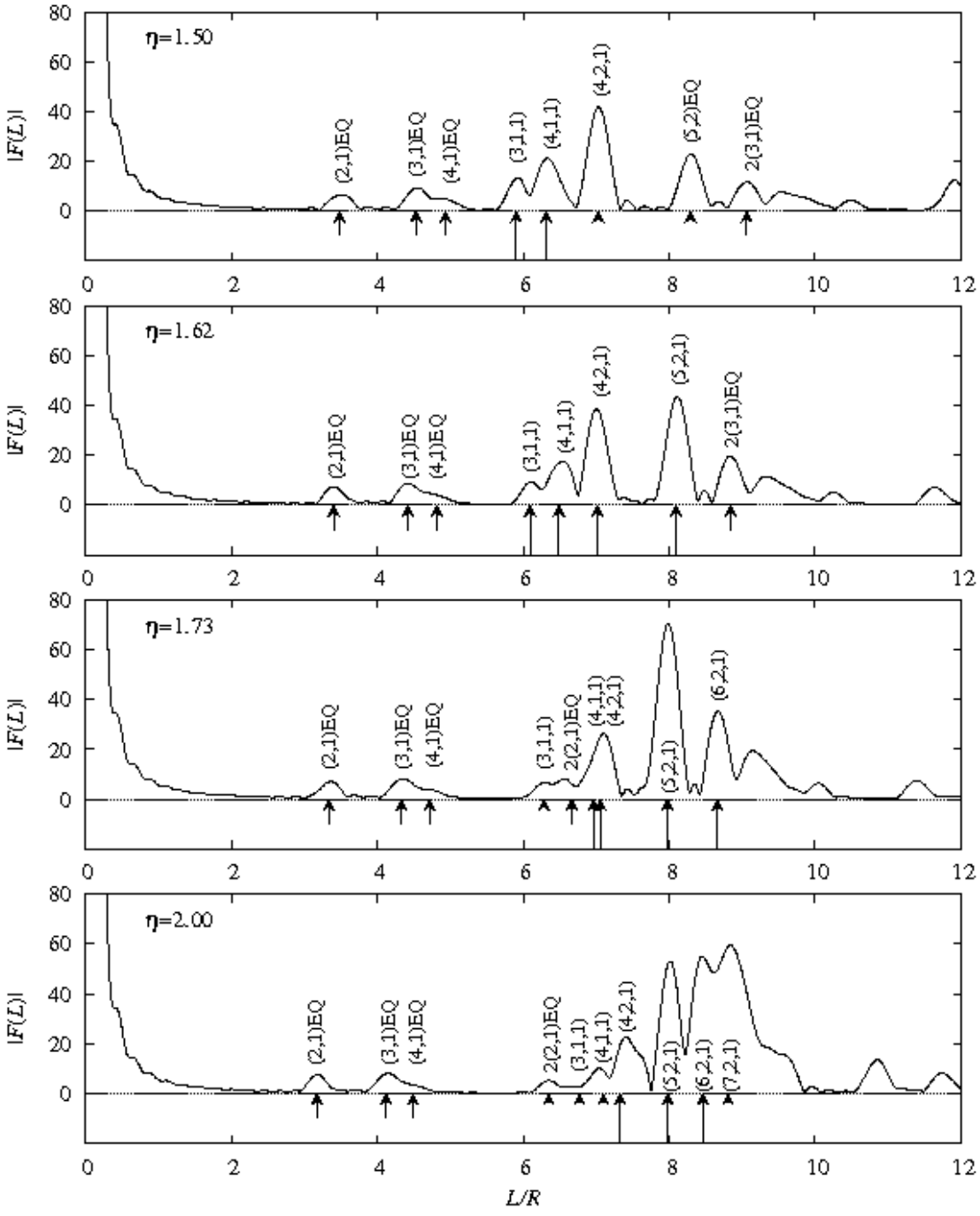


Figure 22: Fourier transform $|F(L)|$ (14) of the quantum level density $g(k)$ of the spheroidal cavity, plotted vs. length variable L at the critical deformations $\eta = 1.5$, 1.62, 1.73 and 2.0. It shows a correspondence to the lengths of classical periodic orbits and clear dominance of longer bifurcated period-two POs above the shortest period-one POs: arrows near the peaks mark the lengths of the most important POs; some peaks at the bifurcation deformations show the sum of both newborn and parent bifurcating orbits like in Fig. 6.

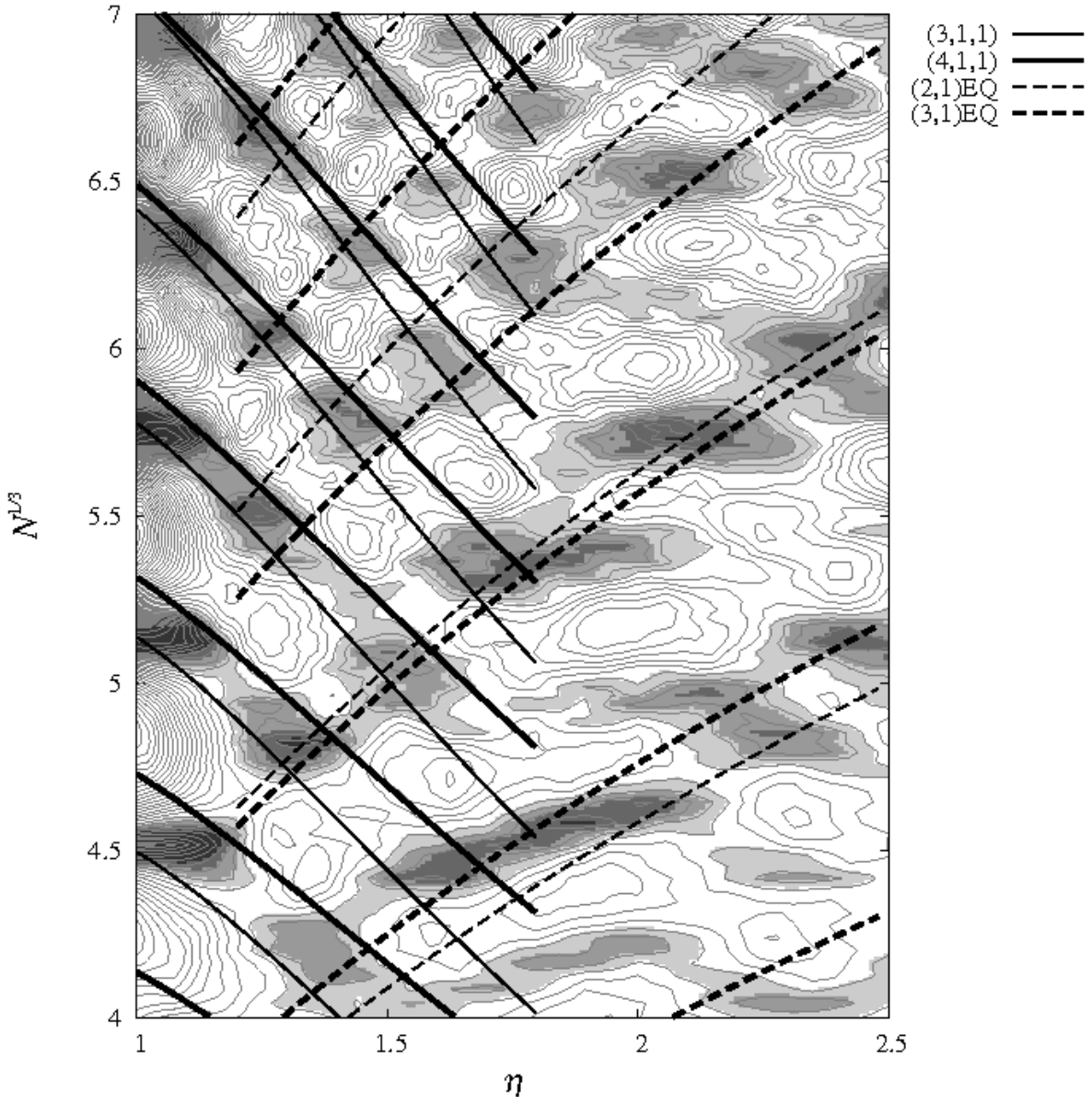


Figure 23: Contour map of shell correction energy δE of the spheroidal cavity versus deformation η and cube-root of particle number $N^{1/3}$. Thick and thin solid lines represent constant-action curves of the classical shortest meridian POs; thick and thin dashed lines show the shortest EQ POs; all are specified on right and are dominating the periodic-orbit sum for the gross-shell structure.

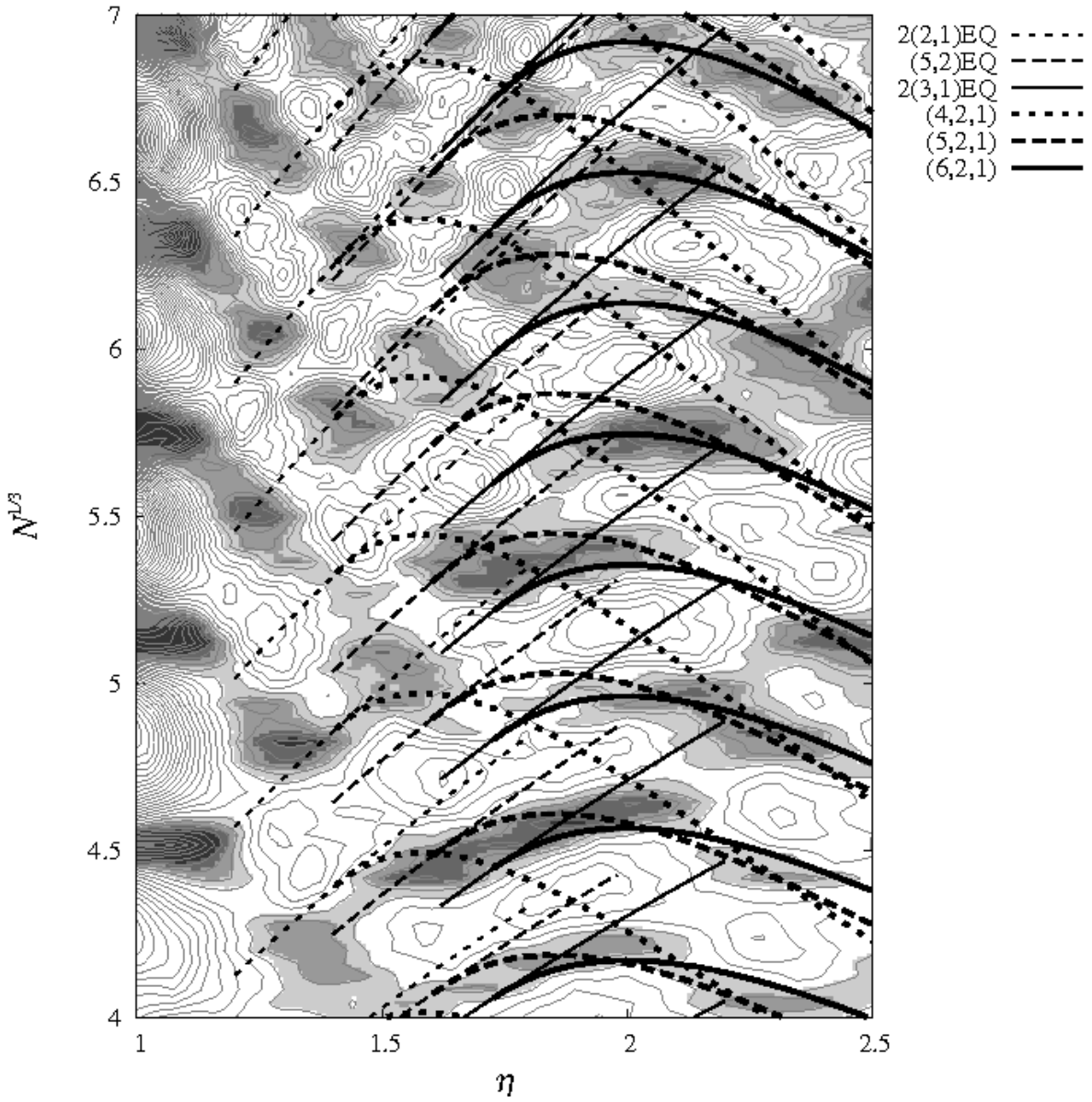


Figure 24: The same as in Fig. 23 but with constant-action lines of the bifurcating POs. Three kinds of curves (dotted, dashed and solid) are shown: Normal and heavy dotted lines present the constant-action curves of the bifurcating 2(2,1)EQ and newborn (4,2,1)2DH orbits; similar dashed lines the (5,2)EQ and (5,2,1)3D orbits, and solid lines show the 2(3,1) and (6,2,1)3D orbits, respectively. All newborn 2DH and 3D orbits dominate the fine shell structure at large enough deformations.

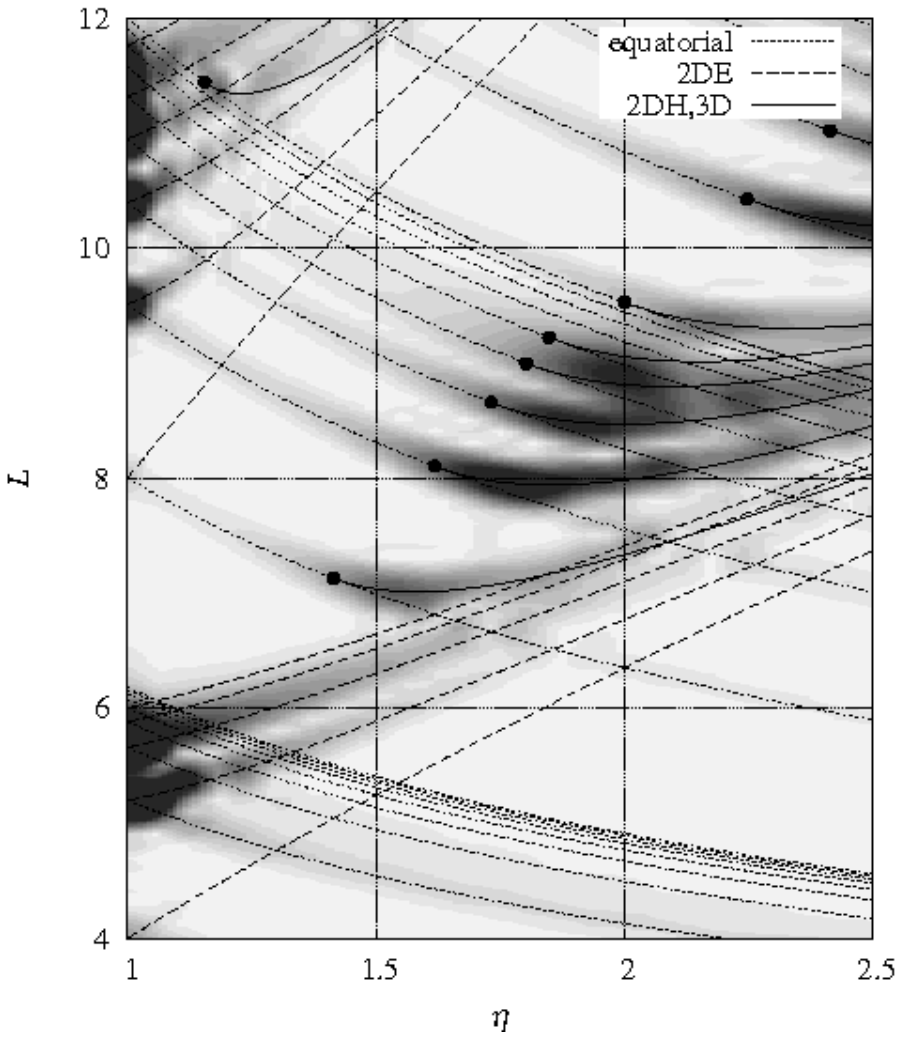


Figure 25: The Fourier transform $|F(L)|$ (14) of the quantum level density $g(k)$ is plotted in grayscale. It shows a clear correspondence to the lengths of classical periodic orbits: dotted curves represent EQ orbits, and dashed curves stand for meridional orbits with elliptic caustics 2DE. Solid curves are either meridional orbits with hyperbolic caustics 2DH or 3D orbits, which are generated via period-multiplying bifurcations of EQ orbits. The black dots show the bifurcation points.

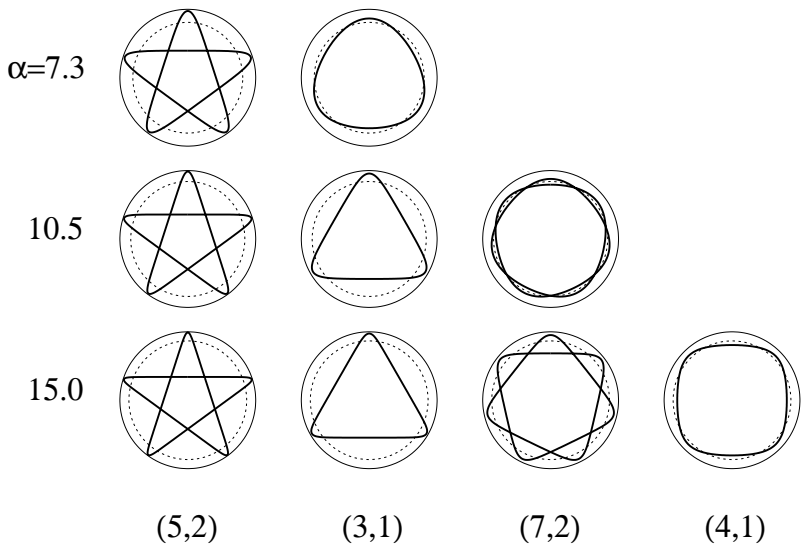


Figure 26: Some short periodic orbits in the power-law potential (23) for several values of α.

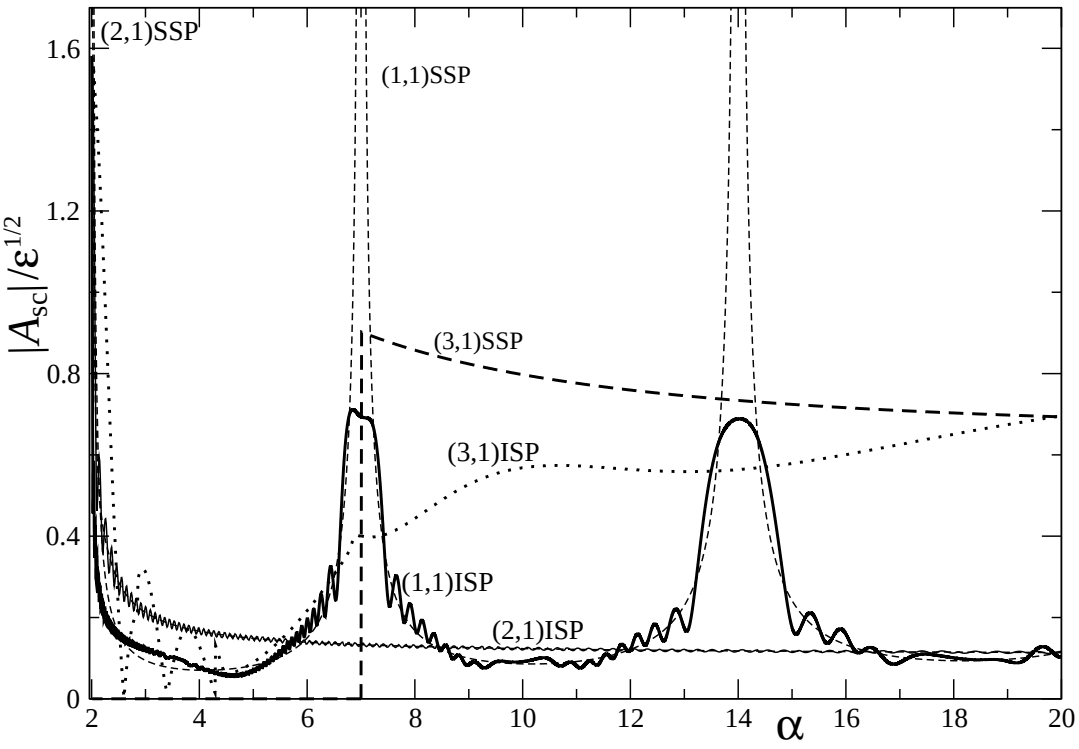


Figure 27: The scaled amplitudes $|A_{sc,po}|$ as functions of α for the once repeated ($M = 1$) circular [$(1, 1)$, see (30)], one-repeated ($M = 1$) diameter $(2, 1)$ and triangle PO $(3, 1)$, in units of $\varepsilon^{1/2}$ at the scaled energy $\varepsilon = 10$. Dashed thin (circular (1,1)SSP, diameter (2,1)SSP) and thick (3,1)SSP lines are SSPM results, and solid (thick circular (1,1)ISP and thin diameter (2,1)ISP) as well as dotted (3,1)ISP lines are ISPM results.

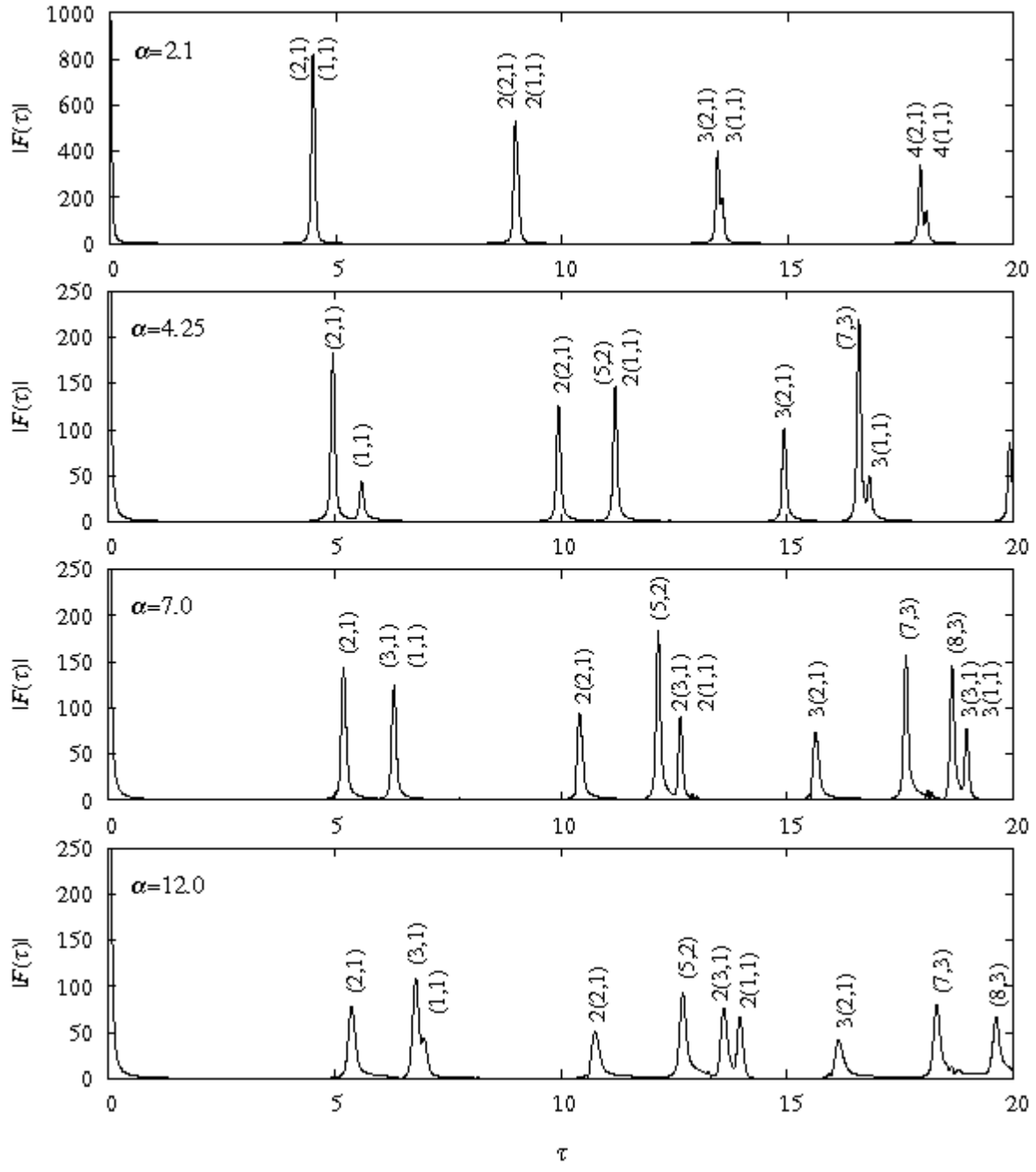


Figure 28: Moduli of the Fourier transform $|F(\tau)|$ of the energy-scaled quantum level density (30), plotted for several values of α.

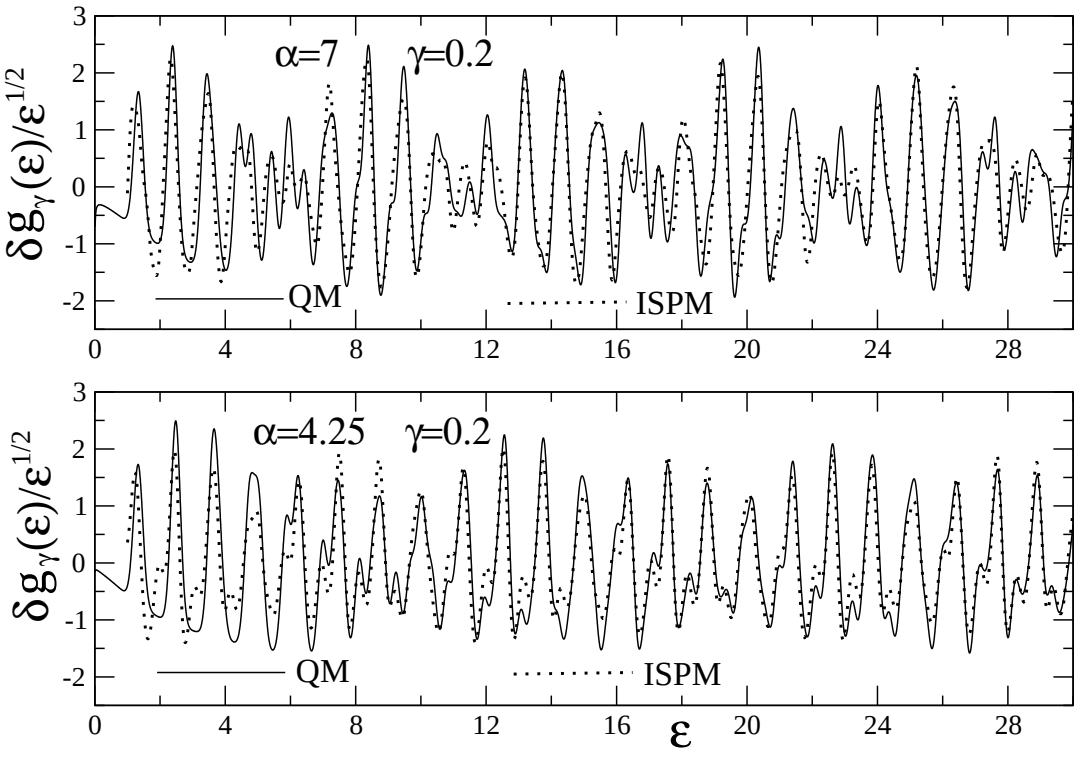


Figure 29: Oscillating part of scaled level density versus scaled energy ε at the bifurcation points $\alpha = 7$ and 4.25 in units of $\varepsilon^{1/2}$. QM (solid line) is the quantum-mechanical result (using Strutinsky averaging with parameters $\widetilde{\gamma} = 3$, $\mathcal{M} = 6$); ISPM (dotted line) is the semiclassical result. In both cases, a (dimensionless) width $\gamma = 0.2$ was used in the Gaussian coarse-graining over the scaled energies.

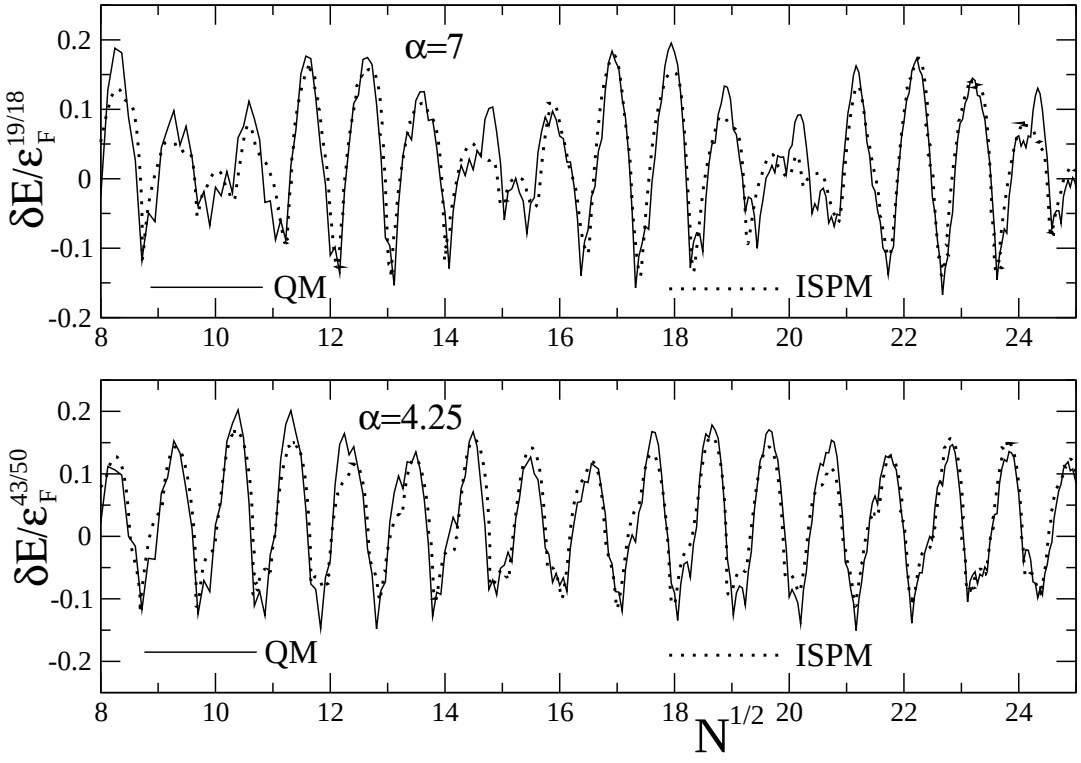


Figure 30: Shell-correction energy δE vs. particle number parameter $N^{1/2}$ at $\alpha = 7$ and 4.25 in units $\varepsilon^{3(\alpha-2)/[2(\alpha+2)]}$. QM (solid line) is the quantum-mechanical result using the shell-correction method (Strutinsky averaging as in Fig. 29 above); ISPM (dotted line) is the semiclassical result using a small coarse-graining width $\gamma = 0.1$ in the calculation of $N(\varepsilon_F)$ by (34) and (25).

References

[1] V. M. Strutinsky, Nucl. Phys. A **95**, 420 (1967); Nucl. Phys. A **122**, 1 (1968).

[2] G. G. Bunatian, V. M. Kolomietz and V. M. Strutinsky, Nucl. Phys. A **188**, 225 (1972).

[3] A. B. Migdal, *The Finite Fermi-System Theory and properties of atomic nuclei* (Nauka, Moscow, 1983, in Russian).

[4] M. Brack and R. K. Bhaduri: *Semiclassical Physics* (revised edition: Westview Press, Boulder, USA, 2003).

[5] V. M. Strutinsky, A. G. Magner, S. R. Ofengenden and T. Døssing, Z. Phys. A **283**, 269 (1977).

[6] V. M. Strutinsky, Proc. of the International Workshop IAEA-SM-241/C12, *Physics and Chemistry of fission 1979*, Vol. 1, p. 475 (1980).

[7] V. M. Strutinsky, Pramana **33**, 21 (1989).

[8] L. D. Landau, Journ. Exp. and Theor. Phys. **30**, 1058 (1957); **32**, 59 (1957); **35**, 97 (1958).

[9] A. A. Abrikosov, I. M. Khalatnikov, Prog. of Phys. Sci. [Uspekhi fizicheskikh nauk] **66**, 177 (1958).

[10] V. A. Khodel, E. E. Saperstein, Phys. Rep. **92**, 183 (1982).

[11] J. Damgård, H. C. Pauli, V. V. Pashkevich and V. M. Strutinsky, Nucl. Phys. A **135**, 432 (1969).

[12] M. Brack, J. Damgård, A. S. Jensen, H. C. Pauli, V. M. Strutinsky and C. Y. Wong, Rev. Mod. Phys. **44**, 320 (1972).

[13] M. C. Gutzwiller, J. Math. Phys. **12**, 343 (1971);
M. C. Gutzwiller: *Chaos in Classical and Quantum Mechanics* (Springer, New York, 1990).

[14] R. Balian and C. Bloch, Ann. Phys. (N. Y.) **69**, 76 (1972); and earlier papers quoted therein.

[15] V. M. Strutinsky, Nukleonika (Poland) **20**, 679 (1975);
V. M. Strutinsky and A. G. Magner, Sov. J. Part. Nucl. **7**, 138 (1976) [Elem. Part. & Nucl. (Atomizdat, Moscow) **7**, 356 (1976)].

[16] M. V. Berry and M. Tabor, Proc. Roy. Soc. London **A349**, 101 (1976);
J. Phys. A **10**, 371 (1977).

[17] S. C. Creagh and R. K. Littlejohn, Phys. Rev. A **44**, 836 (1990); J. Phys. A **25**, 1643 (1992).

[18] A. G. Magner, S. N. Fedotkin, K. Arita, T. Misu, K. Matsuyanagi, T. Schachner, and M. Brack, Prog. Theor. Phys. **102**, 551 (1999).

[19] A. G. Magner, S. N. Fedotkin, K. Arita, K. Matsuyanagi, and M. Brack, Phys. Rev. E **63**, 065201 (2001).

[20] A. G. Magner, S. N. Fedotkin, K. Arita, K. Matsuyanagi, Prog. Theor. Phys. **108**, 853 (2002).

[21] A. G. Magner, K. Arita, S. N. Fedotkin, Prog. Theor. Phys. **115**, 523 (2006).

[22] M. V. Fedoryuk, Sov. J. Com. Math. and Math. Phys. **2**, 145 (1962); **4**, 671 (1964).

[23] M. P. Maslov, Theor. and Math. Phys. **2**, 30 (1970).

[24] M. V. Fedoryuk: *The saddle-point method* (Nauka, Moscow, 1977, in Russian).

[25] M. V. Fedoryuk: *Asymptotics: Integrals and sums* (Nauka, Moscow, 1987).

[26] M. Brack, S. M. Reimann, and M. Sieber, Phys. Rev. Lett, **79**, 1817 (1997).

[27] A. G. Magner, S. N. Fedotkin, F. A. Ivanyuk, P. Meier, M. Brack, S. M. Reimann, and H. Koizumi, Ann. Physik, **6**, 555 (1997).

[28] K. Arita, Int. Journ. of Mod. Phys. E **13** 191 (2004).

[29] V. M. Strutinsky, Yad. Fiz. **3**, 614 (1966) [Sov. J. Nucl. Phys. **3**, 449 (1966)].

[30] S. A. E. Johansson, Nucl. Phys. **22**, 529 (1962).

[31] S. G. Nilsson, Mat.-Fys. Medd. Dan. Vid. Selsk. **29**, no. 16 (1955);
B. R. Mottelson and S. G. Nilsson, Phys. Rev. **99**, 1615 (1955); Mat.-Fys. Skr. Dan. Vid. Selsk. **1**, no. 8 (1959).

[32] N. Bohr and J. A. Wheeler, Phys. Rev. **56**, 426 (1939).

[33] S. Cohen and W. J. Swiatecki, Ann. Phys. (N. Y.) **22**, 406 (1963).

[34] L. Wilets: *Theories of nuclear fission* (Clarendon Press, Oxford, 1964).

[35] W. D. Myers and W. J. Swiatecki, Ann. Phys. (N. Y.) **55**, 395 (1969).

[36] S. M. Polikanov, V. A. Druin, V. A. Karnaukhov, V. L. Mikheev, A. A. Pleve, N. K. Skobelev, V. G. Subbotin, G. M. Ter-Akop'yan, and V. A. Fomichev, Sov. Phys. JETP **15**, 1016 (1962).

[37] V. M. Strutinsky, Ark. Fys. **36**, 629 (1967).

[38] W. D. Myers and W. S. Swiatecki, Nucl. Phys. **81**, 1 (1966).

[39] A. Sobiczewski, A. Gyurkovich, and M. Brack, Nucl. Phys. **A 289**, 346 (1977).

[40] F. A. Ivanyuk and V. M. Strutinsky, Z. Phys. **A 293**, 337 (1979), and earlier refs. quoted there.

[41] K. Pomorski, Phys. Rev. C **70**, 044306 (2004).

[42] M. Centelles, P. Lebouef, A. G. Monastra, J. Roccia, P. Schuck, and X. Vinas, Phys. Rev. C **74**, 034332 (2006).

[43] J. Roccia and P. Leboeuf, Phys. Rev. C **76**, 014301 (2007).

[44] H. A. Bethe, Ann. Rev. Nucl. Sci. **21**, 93 (1971).

[45] E. Werner, K. M. Dietrich, P. Möller, and R. Nix, in: *Physics and Chemistry of Fission 1973* (IAEA Vienna, 1974), Vol. I, p. 501.

[46] For a review, see M. Brack and P. Quentin, Nucl. Phys. A **361** (special volume in commemoration of Sven Gösta Nilsson), p. 35 (1981).

[47] C. Yannouleas and U. Landman, Phys. Rev. B **48**, 8376 (1993).

[48] S. M. Reimann, S. Frauendorf and M. Brack, Z. Phys. D **34**, 125 (1995).

[49] S. Frauendorf and V. V. Pashkevich, Ann. Phys. (Leipzig) **5**, 34 (1996).

[50] V. V. Pashkevich, P. Meier, M. Brack and A. V. Unzhakova, Phys. Lett. A **294**, 314 (2002).

[51] D. Ullmo, T. Nagano, S. Tomsovic and H. Baranger, Phys. Rev. B **63**, 125339 (2001).

[52] M. V. Berry and K. E. Mount, Rep. Prog. Phys. **35**, 315 (1972).

[53] J. Kaidel, M. Brack, and P. Winkler, Phys. Rev. E **70**, 066208 (2004).

[54] S. Frauendorf, Physica Scripta, T **125**, 1 (2006).

[55] A. G. Magner, A. S. Sitdikov, A. A. Khamzin and J. Bartel, Phys. Rev. C **81**, 064302 (2010).

[56] K. Arita and M. Brack, J. Phys. A **41**, 385207 (2008).

[57] S. Reimann, M. Brack, A. G. Magner, J. Blaschke and M. V. N. Murthy, Phys. Rev. A **53**, 39 (1996).

[58] M. Brack, J. Blaschke, S. C. Creagh, A. G. Magner, P. Meier, and S. M. Reimann, Z. Phys. D **40**, 276 (1997).

[59] S. Frauendorf, V. M. Kolomietz, A. G. Magner, and A. I. Sanzhur, Phys. Rev. B **58**, 5622 (1998).

[60] M. Brack, M. Ögren, Y. Yu and S. M. Reimann, J. Phys. A **38**, 9941 (2005).

[61] P. Möller and S. G. Nilsson, Phys. Lett. **31 B**, 283 (1970).

[62] H. C. Pauli, T. Ledergerber, and M. Brack, Phys. Lett. **34 B**, 264 (1971).

[63] C. Gustafsson, P. Möller, and S. G. Nilsson, Phys. Lett. **34 B**, 349 (1971).

[64] M. Brack, P. Meier, S. M. Reimann, and M. Sieber, in: *Similarities and differences between atomic nuclei and clusters*, eds. Y. Abe *et al.* (American Institute of Physics, 1998) p. 17.

[65] M. Brack, M. Sieber, and S. M. Reimann, in: *Nobel Symposium on Quantum Chaos*, eds. K.-F. Berggren and S. Åberg; Physica Scripta **T90**, 146 (2001).

[66] G. Littlejohn and W. G. Flynn, Phys. Rev. A **44**, 5239 (1991); *ibid.* A **45**, 7697 (1992).

[67] J. Bolte and S. Keppeler, Ann. Phys. (N. Y.) **274**, 125 (1999).

[68] M. Pletyukhov, Ch. Amann, M. Mehta, and M. Brack, Phys. Rev. Lett. **89**, 116601 (2002); M. Pletyukhov and O. Zaitsev, J. Phys. A **36**, 5181 (2003).

[69] M. Brack, Ch. Amann, M. Pletyukhov, and O. Zaitsev, Int. J. Mod. Phys. E **13**, 19 (2004).

[70] Ch. Amann and M. Brack, J. Phys. A **35**, 6009 (2002).

[71] H. Olofsson, S. Åberg, and P. Leboeuf, Phys. Rev. Lett. **100**, 037005 (2008);
S. Åberg, H. Olofsson, and P. Leboeuf, AIP Conf. Proc. **995**, 173 (2008).

[72] M. Brack and J. Roccia, Int. J. Mod. Phys. E **19**, 725 (2010); see, in particular, Sect. 4.

[73] M. Brack and K. Tanaka, Phys. Rev. E **77**, 046205 (2008).